Organisation of the orthobunyavirus tripodal spike and the structural changes induced by low pH and K^+ during entry

Samantha Hover[1,2], Frank W Charlton[1,2], Jan Hellert[3], John N Barr[1,2*], Jamel Mankouri[1,2*], Juan Fontana[1,2*]

[1]School of Molecular and Cellular Biology, [2]Astbury Centre for Structural and Molecular Biology, University of Leeds, LS2 9JT, United Kingdom.

[3]Centre for Structural Systems Biology, Leibniz-Institut für Virologie (LIV), Notkestraße 85, 22607 Hamburg, Germany.

*Correspondence: **Dr Juan Fontana** Tel: +44 (0)113 343 4170, Fax: +44 (0)113 343 4803, Email: J.Fontana@leeds.ac.uk; **Dr John N. Barr** Tel: +44 (0)113 343 8069 Email: J.N.Barr@leeds.ac.uk; **Dr Jamel Mankouri,** Email: bms9jm@gmail.com

Author contributions: Experimental work performed by SH; grid preparation by SH and JF; computational analysis by SH, JF, FC and JH; experimental design by SH, JF, JM and JB; manuscript preparation by SH, JF, JM and JB, with input from all authors.

Keywords: Virus, potassium, bunyavirus, endosome, priming, fusion, glycoprotein, cryo-electron tomography, subtomogram averaging.

Classification: Biological sciences

Running Title: Structural conformations of the BUNV glycoproteins

Abstract

Following internalisation, viruses employ the changing environment of maturing endosomes as cues to promote endosomal escape, a process mediated by viral glycoproteins. Specifically, we previously showed that both high [K^+] and low pH promote entry of Bunyamwera virus (BUNV), the prototypical bunyavirus. Here, we used sub-tomogram averaging combined with AlphaFold, to generate a pseudo-atomic model of the whole glycoprotein envelope of BUNV. This allowed us to unambiguously locate the Gc fusion domain and its chaperone Gn within the floor domain of the spike. We also confirmed that low pH and high [K^+] alters the viral glycoproteins, resulting in an activated intermediate state functionally-distinct from the highly ordered ground state, and we localize these changes to the floor domain. Biochemical data suggests that in this intermediate state the viral fusion loops are partially exposed and selectively interact with host cell membranes. Taken together, we reveal new mechanistic understanding of the requirements for virus entry.

Introduction

The *Bunyavirales* order is the largest collection of enveloped negative-sense RNA viruses with over 500 named isolates. Within this group, members of the *Hantaviridae*, *Nairoviridae*, *Phenuiviridae* and *Peribunyaviridae* families possess tri-segmented genomes (1) that minimally encode an RNA-dependent RNA-polymerase, two viral glycoproteins (GPs) Gn and Gc, which form spikes projecting from the viral envelope, and a nucleocapsid (N) protein that encapsidates the genomic segments forming ribonucleoproteins (2). Several members of these families are serious human pathogens, although no vaccines or antiviral therapies to prevent their associated disease have been approved (3,4).

Bunyaviruses enter cells through the endocytic system, releasing their genomes following fusion between their envelope and vesicular membranes, mediated by the Gn/Gc spikes, which together comprise the fusion machinery. The cues that trigger fusion result from endosomal maturation, which might involve a gradual drop in intraluminal pH, changes in concentrations of other ions or

48 alterations to the lipid and protein composition of endosomal membranes (5), dictating when and
49 where fusion occurs. This prevents premature fusion in inappropriate compartments, which would
50 jeopardize virus entry and infection (6).

51 For bunyaviruses, the events that lead to spike fusogenesis are not completely characterised. Many
52 bunyaviruses require low pH to induce a fusogenic state and, for some, a high H^+ concentration has
53 been proposed to be sufficient to establish post-fusion conformations *in vitro* and trigger interactions
54 with liposomes (7–9). Working with the model peribunyavirus, Bunyamwera virus (BUNV), and the
55 model nairovirus, Hazara virus (HAZV), we recently showed the current description of bunyavirus
56 entry is over-simplistic. We showed the concentration of K^+ ions ([K^+]) in endosomes, which is
57 controlled by cellular K^+ channels and increases as endosomes mature, peaking in late endosomes
58 (Fig. 1a), is an important cue for BUNV and HAZV entry. By blocking K^+ channels
59 pharmacologically, we showed that disruption of endosomal K^+ accumulation impedes bunyavirus
60 infection by preventing endosomal release, and instead viruses were trafficked to lysosomes, where
61 they were degraded (10), a mechanism that was also interlinked with cellular cholesterol levels (10–
62 12). For HAZV, we further showed that treatment with elevated K^+ alone (pH 7.3) was sufficient to
63 trigger conformational changes in the GP spikes to induce interactions with co-purified vesicles (13).
64 However, the low resolution of our subtomogram average (STA) and the lack of atomic models for
65 HAZV GPs prevented a detailed structural understanding of the effect of K^+ on the GPs. Of note, it
66 has recently been shown that disruption of the cellular K^+ gradient using KCl or the K^+ ionophore
67 valinomycin inhibits infection by the peribunyaviruses La Crosse virus (LACV), keystone virus and
68 Germiston virus; and of the phenuivirus RVFV (14,15), suggesting that K^+ is broadly required during
69 bunyavirus entry.

70 Here, we used cryo-electron microscopy (cryo-EM) and tomography (cryo-ET) to unravel the
71 structure of the envelope of BUNV and to identify changes in the virion architecture at endosomal
72 pH and [K^+]. STA was performed to generate an average of the BUNV GPs that allowed us to fit
73 published atomic models of specific regions of Gc (16), and identify the position of the fusion
74 domain of Gc, and of Gn. Modelling both GPs (Gn and Gc) using AlphaFold (17) allowed us to

75 generate a full pseudo-atomic model of the GP envelope of BUNV. Furthermore, we hypothesised
76 that K^+ triggers BUNV GPs similar to HAZV, causing conformational changes in the distinctive
77 tripodal GP spikes, to elicit a fusion-competent state (13). STA of pH 6.3/K^+ treated virions revealed
78 drastic changes and an uncoupling of Gn-Gc hetero-hexamers. Consistent with these structural
79 data, biochemical assays confirmed that structural changes elicited by K^+ are localised to the so-
80 called 'floor region' of the GP spikes. pH 6.3/K^+ treated viruses also interacted more readily with
81 target membranes, suggesting these conditions prompt exposure of the fusion loop as an
82 intermediate step of the GPs prior to fusion triggering.

83 **Results**

84 **pH 6.3 and K^+ alter the BUNV GPs to expedite infection**

85 We are interested in the structural and functional changes of bunyavirus GPs in response to
86 biochemical cues during entry. In our previous studies, we showed that the pH and K^+ dependence
87 of virus entry can be recapitulated *in vitro* (termed 'priming'), where exposing virions to
88 physiologically relevant endosomal [H^+] and [K^+], at 20 mM or higher, led to accelerated onset of
89 infection (10). Here, we aimed to untangle the effects of low pH and K^+. Of note, when treating
90 viruses at pH 6.3, the addition of K^+ resulted in a dramatic change in the amount of NP observed at
91 18 hpi, and suggested a distinct role for K^+ during entry (10). As the GPs are key mediators of
92 multiple stages of viral entry, we modified the *in vitro* priming assays (10) to assess the effects of K^+
93 treatment on GP interactions with host membranes. WT BUNV did not bind strongly to surface
94 receptors at 4 ºC (to block endocytosis), with PBS or trypsin washes capable of removing bound
95 virus (Supplementary Fig. 1a). Virions were then treated at pH 6.3/K^+ (+) or pH 6.3/no K^+ (-) (or a pH
96 7.3/no K^+ treated control (Ctl)), and their binding to host cells assessed. Unbound virions were then
97 removed by washing, and infection was allowed to proceed for 24 h (Fig 1b). A timepoint of 18 hpi
98 was also used to confirm the effects of priming, where K^+ treated virions would be expected to
99 initiate infection more quickly, showing higher levels of BUNV-N expression (Fig. 1c, lanes 1-2);
100 however, BUNV-N normalises to similar levels as the no-K^+ treatment by 24 hpi (Fig. 1c, lanes 6-7;

101 as previously described (10)). Importantly, in control and pH 6.3/no K^+ treated viruses, little-to-no
102 BUNV-N was detectable at 24 hpi when virions were washed after binding at 4 ºC, indicating that
103 the washing steps efficiently removed bound virions from the cell surface (Fig. 1c, lanes 3-4). In
104 contrast, BUNV-N was detected at similar levels to the unwashed viruses when virions were pre-
105 treated at pH 6.3/K^+, indicating that these virions bind more strongly to host cell membranes and/or
106 receptors, and are less readily removed by washing (compare Fig. 1c, lane 5 to lanes 3-4).

107 We also tested the ability of virions to fuse with the plasma membrane under pH 6.3 conditions
108 using acid-bypass assays (18), using acidic buffers to induce fusion at the plasma membrane and
109 pharmacologically inhibiting endocytic entry (10,12) (Supplementary Fig. 1b). To confirm the effects
110 of pH 6.3/K^+ during the 2 min of the acid-bypass on viral infection, BUNV-N expression was
111 assessed at 18 hpi and an increase was evident in response to K^+, albeit at reduced levels, likely
112 owing to the short duration of treatment (2 min versus 2 hrs in 'priming' assays above)
113 (Supplementary Fig. 1c). Of note, at 24 hpi, a small BUNV-N band was detected for the bypass at
114 pH 6.3/K^+ in the presence of drugs that was not present in the no-K^+ condition, indicating that
115 pH 6.3/K^+ virions can bypass endocytosis and fuse at the cell membrane. Together, these data
116 indicate that K^+ at pH 6.3 acts upon the BUNV GPs increasing interactions with target membranes,
117 potentially by exposing the fusion loops.

118 **K^+ acts upon the floor region of BUNV GPs**

119 For BUNV, a low resolution structure of the BUNV Gn-Gc (~30 Å) previously revealed an unusual
120 tripod-like structure of the GPs, forming a local lattice-like arrangement of trimers on the virus
121 surface (19). Three regions of the GP tripod were termed the head (apex of the tripod; viral
122 membrane-distal), stalk (connects head-floor) and the floor region (membrane-proximal). More
123 recently, it was identified that the head and stalk regions were formed by the first half of the Gc
124 ectodomain by solving the crystal structures of the head and stalk domains from the
125 peribunyaviruses BUNV (head domain) and Schmallenberg virus (SBV; head-stalk domains) (16).
126 The membrane-proximal floor region is therefore predicted to contain the remaining half of the Gc
127 ectodomain, which includes the fusion domain, and the entire Gn ectodomain.

128 To identify the region in which K^+ is acting, we utilised a recombinant BUNV which has the Gc head
129 and ~70% of the stalk replaced with eGFP (GFP-BUNV; Fig. 1d) (20). We hypothesised that if this
130 mutant virus can be triggered by pH 6.3/K^+ and expedite infection similar to the pH 6.3/K^+ treated
131 WT BUNV, K^+ must act on the floor region, as this is the only common component between GPs
132 from WT BUNV and GFP-BUNV. Indeed, this was the case, as evidenced by increased GFP-BUNV-
133 N expression at 18 hpi after pH 6.3/K^+ treatment (Fig. 1e-f). At this timepoint GFP-BUNV mimicked
134 WT BUNV whereby the presence of K^+ at pH 6.3 was able to expedite infection significantly
135 compared to the pH 6.3/no K^+, and to a greater extent than the pH 7.3/no K^+ control; as previously
136 described for WT (10). This effect on the GFP-BUNV suggests that K^+ is acting upon the floor
137 region, i.e. Gn and/or the fusion domain of Gc, to increase the efficiency of the fusion machinery.
138 Together with the previous finding that the C-terminal portion of Gc is essential for virus infection
139 (21), this indicates that the floor domain of the envelope is the main determinant for virus entry.
140 However, understanding the architecture and function of the floor region required more structural
141 detail than what was currently available.

142 **Acidic pH and K^+ alter the architecture of BUNV virions preventing virion aggregation**

143 To investigate the effects of K^+ and pH on BUNV GPs by cryo-EM, virus growth and purification
144 conditions were optimised from previously described protocols (19,22). Briefly, BHK-21 cells were
145 infected with BUNV, viral supernatants were collected, concentrated by ultracentrifugation, and
146 titred by plaque assay (Supplementary Fig. 2a-c). SDS-PAGE and negative stain EM of purified
147 BUNV confirmed high viral titres and low background contamination, as required for cryo-EM
148 (Supplementary Fig. 2d,e). To characterise the structural effects of pH and K^+, purified virions were
149 treated as above at both pH 7.3 and pH 6.3, and with K^+, prior to vitrification by rapid freezing.

150 2D cryo-EM micrographs of pH 7.3/no K^+ treated virions revealed roughly spherical virions in which
151 the lipid bilayer was clearly identifiable surrounding an electron-dense core, likely due to the
152 presence of tightly packed ribonucleoproteins (Fig. 2a; widefield micrographs of cryo-EM images are
153 in Supplementary Fig. 3a-d); as previously described (19). These features were also observed in
154 pH 7.3/K^+ treated virions (Fig. 2b), though these exhibited a more pleomorphic shape, suggesting

155 structural differences under these conditions or stresses on the virions. At pH 6.3/no K^+, the
156 morphology of the virions was altered and most virions were forming clusters (Fig. 2c), suggestive of
157 direct interactions between virus particles. In some cases, interacting virions were observed with
158 flattened envelopes adjacent to the interaction site (Fig. 2c, white arrowheads, bottom panels),
159 whereas in other cases, membranes were seen to curve around a neighbouring virion (Fig. 2c,
160 black arrowheads, top panel). We reasoned these interactions may have been driven by exposure
161 of the fusion loops of Gc on one virion contacting neighbouring virions, leading to clustering.
162 Intriguingly, virions at pH 6.3/K^+ formed no such clusters and appeared as individual virions
163 (Fig. 2d), suggesting that K^+ prevents the direct interaction of GPs with other viruses thereby
164 preventing clustering at pH 6.3. Taken together, these data suggest that K^+ has a direct effect on
165 virion morphology and GP architecture and function, beyond that elicited by acidic pH.

166 **Cryo-ET reveals an altered GP arrangement in pH 6.3/K^+ virions**

167 We next employed cryo-ET, which allows 3D imaging of pleomorphic specimens, to characterise the
168 morphology of virions treated in conditions mimicking the extracellular environment (pH 7.3/no K^+)
169 and late endosomes (pH 6.3/K^+) (Fig. 1a) (35). pH 7.3/no K^+ virions contained an electron-dense
170 core and a continuous arrangement of GPs on the viral surface (Fig. 2e). In contrast, the pH 6.3/K^+
171 virions were noticeably more pleomorphic, with clear disruption to the regular GP arrangement
172 (Fig. 2f). Areas of GP-free membrane were also evident on the majority of pH 6.3/K^+ virions. These
173 data suggested that pH 6.3/K^+ induced disruption to the local GP arrangements and allows GPs to
174 move more freely and polarise towards one side of the viral membrane and/or that the virus sheds
175 GPs. This polarisation may occur in preparation for interaction with target membranes, leaving large
176 areas of the envelope devoid of GPs.

177 In our tomograms, both the tripodal structure and local trimeric lattice were easily identifiable on
178 pH 7.3/no K^+ virions (Fig. 2g,h). However, pH 6.3/K^+ virions showed a clear disruption of this
179 arrangement and minimal evidence of tripods (Fig. 2i,j), resembling the disruption previously
180 observed in 2D cryo-EM at pH 5.1 (19). Serial sections through individual virions recapitulated these
181 findings; a clear difference was observed in GP architecture and virion morphology between both

182 conditions (Supplementary Fig. 2e,f). Of note, there were no obvious differences in the cores of the
183 virions, suggesting that the effect(s) of pH 6.3/K^+ were limited to viral GPs. Taken together, these
184 data confirm that treatment at pH 6.3/K^+ leads to drastic changes in the GP structure of BUNV.

185 **An improved STA of the BUNV GP permits modelling of the Gc and Gn hetero-hexameric**
186 **arrangement**

187 To assess the physiological relevance of the changes induced by pH 6.3/K^+, a higher resolution
188 map of BUNV GP than that available was required. STA was used to align and average pH 7.3/no
189 K^+ GPs, which confirmed the tripodal arrangement, resolved at ~16 Å (by gold-standard (GS)-FSC
190 Supplementary Fig. 4a). In this average, both leaflets of the viral membrane ('M') were clearly
191 defined at the base, with a GP spike projecting ~16 nm from the surface (Fig. 3a,b). This tripod is
192 predicted to constitute a heterohexamer composed of three copies of the smaller Gn (32 kDa, 186
193 residue ectodomain) and three copies of the larger Gc (110 kDa, 910 residue ectodomain) (23)
194 (Fig. 3c). Our STA showed distinguishable head, stalk and floor regions (Fig. 3d,e), and a previously
195 unidentified density protruding from the floor but shielded by the tripod head (Fig. 3d white
196 arrowheads). Fitting of the previously determined X-ray structures of the head (BUNV) and stalk
197 (SBV) domains into our model (Fig. 3f,g) revealed a tight fit corresponding to cross-correlation
198 values of 0.70 and 0.82 for the head and stalk domains, respectively. The fit of the head trimer
199 allowed us to confirm the handedness of the average (Supplementary Fig. 4b,c). By exclusion, the
200 floor domain must contain the conserved class II fusion domain of Gc and Gn, however specific
201 arrangements could not be obtained from this average (Fig. 3d-f gold region and Supplementary
202 Movie 1).

203 To further our understanding of the architecture of this floor domain, STA was performed focused on
204 this region (Fig. 3h,i) and resulted in an average at a slightly improved resolution of ~14 Å, as
205 determined by GS-FSC (Supplementary Fig. 4a). This average is thought to represent a hetero-
206 hexameric assembly of a trimer of Gn and a trimer of the Gc floor region, which includes the fusion
207 domains (Fig. 4a-d). In the floor domain, novel details were identified that were not resolved in the
208 previously published structure (19), highlighting the interconnected organisation of the fusion

209 domains (Fig. 4c,d). Three stalk domains were also resolved, which identify the connections to three
210 independent tripods. A post-fusion structure of the fusion domain for the related peribunyavirus
211 LACV has been recently solved (pdb: 7A57). LACV Gc exhibits a class II fusion domain and shares
212 ~49% amino acid identity and ~69% similarity with the fusion domain of BUNV Gc. We therefore
213 modelled a LACV pre-fusion domain, based on the differences between the pre-fusion and post-
214 fusion conformations observed for other bunyavirus class II fusion domains, which in broad terms
215 involve the rigid-body rearrangement of domain III (Supplementary Fig. 5) (7,24–26). In addition,
216 there was unoccupied density remaining in the floor region that could accommodate a trimer of Gn
217 in the centre, allowing it to contact the Gc fusion domains and the viral membrane (Fig. 4e,f).

218 There are currently no Gn structures available for any peribunyavirus and only a head domain
219 structure available for BUNV Gc. In order to interpret the STA map of the BUNV prefusion spike we
220 generated an AlphaFold model of the entire Gn-Gc complex (Fig. 5a,b) (17,27), which reached an
221 overall high confidence score with an average pLDDT of 79 (predicted local distance difference test,
222 which is a per-residue estimate of its confidence; scores of 70-90 are expected to be modelled well
223 (17)) (Supplementary Fig. 6a,b) with all conserved cysteines forming plausible disulphides. Fitting of
224 the ectodomains of Gn and Gc from the AlphaFold model into our STA of the tripod (Fig. 5c,d)
225 required only minor adjustments of the angles between head and stalk, and between the two stalk
226 subdomains (Supplementary Fig. 6c), and it resulted in only minor clashes at protein contact sites
227 within the floor.

228 At the time the prediction was made, AlphaFold had not yet been trained on the recently published
229 post-fusion structures of the orthobunyavirus Gc fusion ectodomains (pdb:7A57), a circumstance
230 that allowed further validation of the model. Indeed, the individual Gc fusion domains I, II, and III of
231 the model are virtually identical to those of the LACV x-ray structure with RMSD values of 1.08 Å,
232 1.16Å, and 0.95 Å (pruned atom pairs), respectively, and in the model are arranged in the canonical
233 pre-fusion orientations relative to one another. The arrangement of the Gc fusion domain in the floor
234 STA shows that a trimer fits well within this average (Fig. 5e,f), and in a highly similar way to that

235 predicted using the LACV structure with the fusion loops pointing upward underneath the tripod
236 (Fig. 4e,f and Supplementary Movie 1).

237 The Gn AlphaFold model also displays the typical architecture of its orthologs from hantaviruses,
238 phleboviruses, tospoviruses and alphaviruses, which are divided into domain A, β-ribbon, domain B
239 and domain C (28). Similar to Gn from other bunyavirus families, BUNV Gn is formed of β-sheets,
240 corresponding to domains A, C and β-ribbon (28), and sits parallel to domain II of the Gc fusion
241 domain, likely forming numerous stabilising interactions (Fig. 6a). However, the orthobunyavirus Gn
242 is significantly shorter than the orthologues and the model suggests that it lacks the canonical
243 domain B, and instead resides below an additional region from Gc, the stalk (Fig. 6, compare a, b &
244 c). Our unambiguous fit of three Gn-Gc heterodimer models into the triangular floor of the spike also
245 demonstrates that three protomers of Gn trimerize at the centre of the floor in a similar fashion as in
246 the tetrameric hantavirus spike (26) (Fig 6).

247 Overall, the AlphaFold prediction confirms the orientation and positions of both Gn and Gc, and
248 allows us to model the whole orthobunyavirus GP envelope. This arrangement emphasises the role
249 of Gn in stabilising the tripod and the fusion domains in the floor region, and demonstrates how the
250 lattice-like local arrangements are formed (Fig. 5g,h and Supplementary Movie 2).

251 **pH 6.3/K^+ affects the floor region, resulting in GP trimer uncoupling**

252 As we had established an effect of pH 6.3/K^+ on the floor domain of the BUNV GP, we subsequently
253 used STA to determine the GP arrangement from pH 6.3/K^+ virions; resolved to ~16 Å resolution
254 (FSC cut-off of 0.5, Supplementary Fig. 4d). A dramatic change in GP architecture was observed,
255 with the lack of clear tripods and the flexibility of the spikes evident early during processing
256 (Fig. 2f,i,j), suggesting that pH 6.3/K^+ treatment had uncoupled the tripods (Fig. 7a-d). A short spike-
257 like projection was aligned extending from the membrane (~10 nm), with a large, flat region of
258 density above the lipid bilayer, which did not form the regular floor domain structure observed in the
259 pH 7.3/no K^+ condition. The lack of density at the top of the spike was indicative of a highly dynamic
260 unstructured region, exhibiting multiple conformations which cannot be resolved by STA (Fig. 7a,c).

261 However, two features were apparent from these averages: 1) the lack of organised tripods
262 indicates uncoupling of this region, with the 'spike' potentially corresponding to an extended Gc
263 fusion domain or stalk domain from the pH 7.3/no K^+ average (Supplementary Fig. 7); 2) a floor
264 region was present in this average, albeit it did not appear to form the ordered trimeric arrangement
265 at the base of the spike observed for the pH 7.3/no K^+ (Fig. 7d,e and Supplementary Movie 1).
266 Interestingly a monomer of the Gc fusion domain in its pre-fusion conformation did not fit well within
267 this region, indicating that it is likely located within the 'spike' and extended away from the viral
268 membrane (Supplementary Fig. 7).

269 With the lack of observable tripods, we took advantage of a monoclonal anti-Gc neutralising
270 antibody (mAb-742) which recognises a conformational epitope on the head domain (near
271 glycosylation site N624, which resides on the top of the head (Fig. 3c,g, N624 indicated)) (29,30).
272 Western blot for BUNV-N of lysates from cells infected with viruses treated at pH 7.3/no K^+,
273 pH 6.3/no K^+ or pH 6.3/K^+, and incubated with mAb-742, showed that this antibody neutralises
274 infection by all treated virions (Supplementary Fig. 8). This confirms that the head-stalk domains are
275 intact and remain attached after pH 6.3/K^+ treatment; which was unclear from the STA. It is likely
276 that the pH 6.3/K^+ viruses are still neutralised owing to steric hindrance.

277 **Discussion**

278 We previously demonstrated that for BUNV low pH and K^+ treatment, and for HAZV neutral pH and
279 K^+ treatment, expedites infection. However, mechanistic insight using HAZV was limited owing to
280 the low resolution of the STA and lack of GP structures available (10,13) and completely missing for
281 BUNV. Here, we utilised BUNV to investigate the mechanistic and structural consequences of
282 endosomal pH and K^+ during bunyavirus entry using cryo-ET and STA.

283 Using BUNV, orthobunyavirus GPs were previously shown to form a trimeric tripod structure that
284 extends above the membrane-bound floor region, where interactions with neighbouring floor regions
285 generate locally ordered lattice-like arrangements (19). This contrasts the GP organisation for
286 species from other bunyavirus families, which is tetrameric (13,26,31), or icosahedral (32–37).

287 Here we have improved the average of the BUNV trimer, allowing us to fit structures of the BUNV
288 head and SBV stalk, confirming previous predictions that the fusion domain resides in the floor
289 region (Figs. 3,4) (16,19). Our improved resolution of the floor region, coupled with an AlphaFold
290 model of the complete BUNV Gn-Gc dimer, allowed us to model the whole viral envelope and
291 demonstrates the hetero-hexameric 3x(Gn/Gc) assembly (Fig. 5g,h). Additionally, the fitting of Gc in
292 our subtomogram average shows by exclusion that Gn resides at the centre of the floor domain,
293 likely stabilising this region. This assembly resembles the organization of the Alphavirus envelope,
294 in which three protomers of the class II fusion protein E1 laterally surround a trimeric core of its
295 chaperone E2 (38). A similar assembly, with however different stoichiometry, is also found in the
296 hetero-octameric 4x(Gn-Gc) complex of the orthohantavirus envelope (Fig. 6h) (26). In the pre-
297 fusion structures of related fusion machineries (*Phenuiviridae* (RVFV) and *Hantaviridae*
298 (TULV/ANDV)) (26,32), Gn typically overtops Gc and is thus likely involved in shielding the fusion
299 loops and mediating initial contact with the target cells (23,39) (Fig. 6g-i). In contrast however, our
300 model of the BUNV assembly illustrates that orthobunyavirus Gn cannot completely cover the Gc
301 fusion domain. The capping loop found at the tip of Gn is also shorter than that of hantaviruses,
302 however it still partially shields the fusion loops (Fig. 6). In addition to its polypeptide chain, a strictly
303 conserved N-linked glycan on the capping loop (residue N60) is likely maintained to directly interact
304 with the fusion loops on Gc (26) (as indicated in Figs. 3c and 6a). This Gn glycan was previously
305 shown to be essential for correct GP folding and successful virus rescue, suggesting an important
306 function in the regulation of the pre/post-fusion switch (30). An intriguing difference to these
307 orthologous systems is the relatively small size of the orthobunyavirus Gn (~40-60% smaller,
308 ~30 kDa), with Gc also being ~40-50% larger (~110 kDa) (23,40). The unique N-terminal half of
309 larger orthobunyavirus Gc appears to compensate for the small size of its Gn, being well positioned
310 for receptor scavenging and indirectly shielding the fusion machinery (Figs. 5,6 and Supplementary
311 Movie 1). These head and stalk domains of BUNV Gc are dispensable for infection and are not
312 involved in cell fusion or Golgi trafficking, indicating no role in subsequent stages of infection
313 (20,21). Furthermore, our results show that the head and stalk domains are not required for virus
314 triggering by pH 6.3/K^+, indicating a specific effect of this condition on the floor region (Fig. 1d-f).

315 Despite its smaller size, orthobunyavirus Gn likely stabilises the centre of the floor region to
316 maintain the arrangement of the Gc fusion domains, similar to that seen for other bunyavirus
317 glycoproteins.

318 With the Gc tripod and the Gn capping loop including its conserved glycan shielding the fusion
319 loops, disassembly of the tripod is required during fusion, similar to the glycoprotein rearrangement
320 required for exposure of the fusion loops of RVFV, HTNV and ANDV (26,32,41,42). This
321 disassembly is likely caused by a biochemical trigger during entry which would initiate the structural
322 changes in the GPs to expose the fusion loops, permitting their interaction with endosomal
323 membranes. This is what we observed upon pH 6.3/K^+ treatment, where the organised trimeric
324 arrangement is disassembled, and could involve exposure of the fusion loops to target membranes.
325 This is consistent with the K^+ effects previously shown for HAZV, where K^+ treatment triggered large
326 structural changes in the GPs at neutral pH, causing elongation of the GP spikes and their
327 association with co-purified membranes (13). This however differs from previous studies on the
328 BUNV GP trimer that suggested the occurrence of uncoupling at pH 5.1 in the absence of K^+ (19),
329 since shown to render BUNV non-infectious (10), therefore likely representing a post-fusion
330 conformation. As the requirement of K^+ for other bunyaviruses has not been explored, the pH 6.3/K^+
331 induced loss of the hetero-hexameric arrangement observed for BUNV may differ to the loss of the
332 ordered tetrameric arrangement of the TULV (hantavirus) GPs at pH 5.0 (42), or the elongation and
333 membrane interaction of GP spikes of UUKV (phenuivirus) at the same pH (33).

334 We predict that at pH 7.3 (no K^+) the fusion loops are shielded by the tripodal lattice of Gn and Gc
335 (Figs. 3,4). During entry, BUNV reaches an endosomal environment of pH 6.3 and high [K^+] (Fig. 8),
336 this acts as a partial-trigger initiating changes in the floor region and uncoupling of the tripod
337 (Fig. 7), generating an intermediate disordered state. From the whole virion perspective, this
338 pH 6.3/K^+ triggering disrupts the locally ordered lattice, allowing free movement of the GPs on the
339 BUNV envelope and polarisation and clustering of the GPs to permit fusion, at which point areas of
340 the membrane become devoid of spikes (Fig. 2f). This state is capable of interacting specifically with
341 cell membranes (Fig. 1b,c) (but not viral membranes, as pH 6.3/K^+ virions do not interact with each

342 other; Fig. 2d). Similar structural changes in BUNV may also be elicited at low pH alone (pH 6.3/no
343 K^+), which allows interactions with other virions (Fig. 2c). However, the lack of virus-virus
344 interactions in the presence of K^+ at pH 6.3 suggests that K^+ limits the effects of pH and prevents full
345 exposure of the fusion domains. Interestingly, a post-fusion X-ray structure of ANDV Gc at pH 6.5 in
346 the presence of KCl coordinates a K^+ ion within domain II, at glutamate residue E106, which then
347 forms different interactions and a more unstable arrangement (31). Similar may be true for the pH
348 6.3/K^+ BUNV Gc, in which a K^+ ion coordination may affect exposure of the fusion loops. The fact
349 that K^+ prevents virion aggregation, but allows interactions with host membranes (Fig. 1b,c), may
350 represent a requirement for a specific host factor. Similarly for HAZV, K^+ alone was sufficient to
351 induce interactions with membranes, but no fusion events were observed further suggesting the
352 requirement of an unknown host factor (13). Bunyaviruses commonly require additional host factors
353 for fusion events, such as UUKV which requires the presence of a late endosome-resident
354 phospholipid bis(monoacylglycerol)-phosphate, and LACV and DABV which require serine protease
355 activity (33,43).

356 In order to transit into a post-fusion conformation, structural changes may also be required in the
357 head and stalk domains. Given that the mAb-742 neutralising antibody, which targets a
358 conformational epitope on the head domain (30), is still effective against pH 6.3/K^+ treated viruses,
359 we propose that the structure of the head domain is not altered during fusion (Supplementary Fig.
360 8a-c). In this case, the antibody might work by sterically impeding the refolding of BUNV GPs or
361 blocking the fusion loops from physically reaching the target membrane. Further rearrangements of
362 the fusion domain would then be necessary for the subsequent canonical fusion stages involving
363 viral and host membranes being pulled into close contact, followed by fusion (Fig. 8) (23).

364 In summary, we have determined the molecular arrangement of the Gc fusion domain and Gn within
365 the floor domain of the BUNV spike, and additionally resolved drastic structural changes in the GP
366 architecture in response to pH 6.3/K^+, identifying an intermediate fusion state capable of interacting
367 with target membranes. The ability of pharmacological K^+ channel inhibitors to disrupt infection by a
368 number of bunyaviruses from different families (11,13,14,44), alongside the structural changes

369 elicited by K^+ on both BUNV and HAZV, suggests a shared mechanism that could be exploited
370 therapeutically.

371 **Methods**

372 **Cells and viruses**

373 A549 (human alveolar carcinoma epithelial), SW13 (human adrenal cortex carcinoma) and BHK-21
374 (baby hamster kidney) cells were obtained from the European Collection of Cell Cultures (ECACC).
375 Cells were cultured in Dulbecco's modified Eagle's medium (DMEM, Sigma) supplemented with
376 10% foetal bovine serum (FBS), 100 U/ml penicillin and 100 µg/ml streptomycin, and maintained in
377 a humidified incubator at 37 °C, with 5% CO_2. Wild-type BUNV stocks (provided by Professor
378 Richard Elliott, Glasgow Centre for Virus Research) were generated from infected cell supernatants
379 and titre estimated by plaque assay as previously described (10,11). GFP-BUNV stocks were
380 provided by Dr Xiaohong Shi (Glasgow Centre for Virus Research) and encode an eGFP tag in
381 place of residues 478-827 of the BUNV M segment (the Gc head and stalk regions) (20). Wild-type
382 human respiratory syncytial virus A2 strain (HRSV) was obtained from the National Collection of
383 Pathogenic Viruses (NCPV) of Public Health England (PHE) and cultured as previously described
384 (45).

385 **Virus purification**

386 BHK-21 cells were seeded into T175 flasks and infected with BUNV for 3 hrs in FBS-free DMEM
387 (MOI of 0.1). Media was replaced with 2% FBS DMEM and incubated until 44 hpi at 32 ºC. Virus-
388 containing supernatants were clarified by centrifugation and filtration (0.22 µm filter), and then
389 virions were pelleted by ultracentrifugation (150,000 x *g*, 3 hrs, 4 ºC) through a 30% sucrose
390 cushion (46). Virions were resuspended in 0.1x phosphate buffered saline (PBS, 0.1x to dilute the
391 salts) by gentle rocking at 4 ºC overnight. BUNV titres were determined by plaque assay, and purity
392 was determined by silver staining and negative stain EM.

393 **Plaque assays**

394 Plaque assays were performed in SW13 cells as previously described (10). Viral stocks were
395 serially diluted and SW13 cells were infected and overlayed with semi-solid 1.6% carboxy-methyl
396 cellulose. After 6 days the overlay was removed, cells stained with 1% crystal violet and the number
397 of plaques counted to estimate viral titre.

398 **Silver staining**

399 During the BUNV purification 10 µl samples were collected of the pre-ultracentrifugation viral
400 supernatant (snt), the post-ultracentrifugation snt, snt-sucrose interface and sucrose. Samples were
401 resolved by SDS-PAGE alongside 0.5 µl of purified BUNV and 1:100 diluted protein ladder, then
402 fixed and stained following the silver staining kit (GE Healthcare) manufacturer's instructions.

403 **Western blot**

404 At the indicated time points cells were lysed (25 mM glycerol phosphate, 20 mM tris, 150 mM NaCl,
405 1 mM EDTA, 1% triton X-100, 10% glycerol, 50 mM NaF, 5 mM $Na_4O_7P_2$, pH 7.4), and western
406 blotting was performed as previous (10,45). Proteins were resolved by SDS-PAGE and transferred
407 onto polyvinylidene difluoride (PVDF; Millipore) membranes. After blocking in 10% (w/v) milk in
408 TBS-T, the appropriate primary antibodies (sheep α-BUNV-N (1:5000; produced by J N Barr (11)),
409 goat α-HRSV (1:1000; Abcam ab20745), mouse α-GAPDH (1:1000, Santa Cruz sc47724) or mouse
410 α-GFP (1:1000; Santa Cruz sc-9996)) were added at 4 ˚C overnight, followed by the corresponding
411 HRP-conjugated secondary antibodies (Merck α-sheep A3415; α-goat A8919; α-mouse A4416) for
412 1 hr. Labelling was detected using enhanced chemiluminescence (Advansta) and a Xograph
413 processor. Densitometry was performed using ImageJ and statistical significance determined using
414 a one-way ANOVA where $P<0.05$.

415 ***In vitro* priming assays**

416 BUNV 'priming' assays were performed as previously described (10). BUNV was incubated pre-
417 infection at 37 ˚C for 2 hrs in a range of buffers: pH 7.3 (20 mM tris), and pH 6.3 (30 mM bis-tris)

418 with or without 140 mM KCl (final concentration 128 mM KCl) ('K^+' vs 'no-K^+'). Buffer was diluted out
419 with DMEM prior to infection of A549 cells at a MOI of 0.1 for the indicated times (hpi), after which
420 points cells were lysed and BUNV infection assessed by western blot. For the GFP-BUNV, virus
421 was treated with buffers (primed) as with WT BUNV and infection assessed at 18 hpi.

422 For the cell binding assays, after the pre-infection treatment (pH 6.3/no K^+, pH 6.3/K^+, or a no-buffer
423 WT control (Ctl)), buffers were diluted out with cold DMEM and virions added to cells at 4 ˚C for
424 1.5 hrs; to allow binding but prevent internalisation (10). Cells were washed 3x 30 secs with 0.1x
425 PBS or left unwashed, and infection was allowed to proceed until 24 hpi (see Fig. 1b). An 18 hpi
426 control was performed alongside (no wash) and lysed at 18 hpi as an internal control (to confirm the
427 increase in BUNV-N with pH 6.3/K^+ expected at this timepoint). In the initial wash test assay
428 (Supplementary Fig. 1a), A549 cells were infected at 4 ˚C with BUNV (MOI = 0.1) and left unwashed
429 or washed 3x 30 secs with 0.1x PBS or 0.1% trypsin. Infection was assessed by western blot of
430 cells lysed at 24 hpi.

431 For the neutralisation assays, BUNV was treated at pH 7.3/no K^+ (control), pH 6.3/no K^+ or
432 pH 6.3/K^+ as above, then buffer was diluted and virions were neutralised with mAb-742 anti-BUNV-
433 Gc monoclonal antibody (1:10,000; produced in the Professor Richard Elliott lab at the Glasgow
434 Centre for Virus Research (29)) or a dH_2O control for 1 hr with gentle rocking. A549 cells were then
435 infected at an MOI 0.1 for 18 hrs, at which point cells were fixed for immunofluorescence or lysed for
436 western blot. The fixed cells were permeabilised with methanol/acetone, immunofluorescently
437 stained for BUNV-NP (α-sheep Alexa-fluor-594 secondary antibodies; Thermo Scientific A11016)
438 and images taken using an IncuCyte ZOOM live imaging system as previously described (10,45).

439 **Acid-bypass assay**

440 To induce fusion at the plasma membrane, and thus bypass endosomal entry (see Supplementary
441 Fig. 1b), a protocol was adapted from the procedure previously outlined by Stauffer *et al.* (2014)
442 (18). BUNV (MOI 0.1) was bound to A549 cells by addition at 4 ˚C for 1 hr, and unbound virus was
443 then removed with the media. Virions bound to the cell membrane were subjected to acidic buffers,

444 acid-bypass, by adding warm fusion buffers (pH 6.3/no K^+ or pH 6.3/K^+) to cells for a 2 min pulse at
445 37 ˚C (instead of the 2 hrs used for 'priming'), alongside a DMEM infection control. The pH 6.3
446 fusion buffers used were the same as those used for the priming in the above experiments, but
447 additionally containing 0.1x PBS to maintain cell osmolarity. Cells were subsequently washed with
448 cold DMEM and each condition (pH 6.3/no K^+ or pH 6.3/K^+) was treated with or without drugs to
449 prevent endocytic entry. 10 mM tris(2-carboxyethyl)phosphine (TCEP; Sigma) was added to cells for
450 the '+ drugs' wells for 5 mins at 37 ˚C to inactivate non-internalised virions (12), which was then
451 removed and replaced with an acid-bypass 'stop' buffer (DMEM containing 50 mM HEPES (pH 7.3)
452 and 20 mM ammonium chloride (NH_4Cl); Sigma) to prevent entry by endocytosis (10). As such, only
453 virions that bypass the endocytic network and fuse at the plasma membrane would result in a
454 productive infection (10,12). Cells were incubated at 37 ˚C for 24 hrs, then lysed and infection
455 assessed by western blot. For non-drugged control wells ('- drugs') DMEM was added instead of
456 drugs, under the same conditions, and then cells were incubated until 24 hpi; also included were
457 pH 6.3/no K^+ and pH 6.3/K^+ acid-bypass control wells to be lysed at 18 hpi to confirm triggering
458 occurs under these conditions as with priming experiments.

459 **Electron microscopy**

460 Negative stain EM was used to assess the purification of BUNV prior to cryo-EM (as described
461 previously (12)). Briefly, purified BUNV was loaded onto glow-discharged carbon-coated grids and
462 allowed to stand for 30 secs. Grids were washed three times with dH_2O and stained with 1%
463 aqueous uranyl acetate for 10 secs. Images were collected on a FEI Tecnai T12 electron
464 microscope at 120 kV, using a Gatan Ultrascan 4000 charge coupled device camera and operated
465 between -1 µm and -5 µm nominal defocus.

466 For cryo-EM and cryo-ET, 2 µl purified BUNV virions (~6.8 x 10^6 particles) were diluted in 2 µl (1:1)
467 of a range of priming buffers (pH 7.3/no K^+, pH 7.3/K^+, pH 6.3/no K^+, pH 6.3/K^+; final concentration
468 127.5 mM KCl) for 2 hrs at 37 ˚C matching the priming experiments used previously (10). Virions
469 were then mixed with 2 µl of Protein A conjugated with 10-nm colloidal gold (Aurion) as a fiducial
470 marker for tomogram alignment, and 3 µl of the mixture was immediately loaded onto glow-

471 discharged lacey-carbon EM grids. Grids were blotted for 3 secs and vitrified using a Leica EM GP
472 automatic plunge freezer. Cryo-EM micrographs were collected for each condition on an FEI Titan
473 Krios using a Falcon E3C direct electron detector, operated at 300 KeV and at -0.5 to -3.5 µm
474 defocus.

475 **Cryo-ET and image processing**

476 Grids for cryo-ET were prepared as described above and tilt series were collected using a FEI Titan
477 Krios using an energy-filtered (20 eV slit) Gatan K2 XP summit direct electron detector in counting
478 mode (300 KeV), and a Volta phase plate. Tomography 4 (FEI) software was used to collect single-
479 axis tilt series from -60˚ to +60˚, at 2˚ increments. A defocus of - 1 µm was used, at 53,000x
480 magnification, corresponding to a pixel size of 2.72 Å, and an electron dose of ~1.8 e^- per image
481 (total dose per tilt series ~108 $e^-/Å^2$). Each tilt-series projections was pre-processed by motion
482 correction using Relion 3.0, and contrast transfer function (CTF) calculated using Relion 3.0 (gctf)
483 and then corrected using CTF phase-flip (47,48). The IMOD package eTOMO was used to align the
484 projections using the gold fiducials and calculate the 3D reconstructions by weighted back
485 projection (49), with a final pixel size of 5.44 Å after binning by a factor of two. For STA, unbinned
486 tomograms (2.72 Å pixel size) were also generated using only the -30˚ to +30˚ tilt angles (to improve
487 the signal to noise of the resulting tomograms). Representative images were Gaussian Blur 3D
488 filtered using ImageJ.

489 **Subtomogram averaging**

490 PEET (IMOD package) was used for STA (50) and Bsoft for basic image processing (51). Briefly, for
491 both conditions ~200 spikes were initially selected and the spikeInit programme used to calculate
492 initial orientations perpendicular to the viral membrane. These initial orientations were employed to
493 generate an initial reference used for subsequent particle selection.

494 For the pH 7.3/no K^+ STA, the seedSpikes and SpikeInit programmes were used to automatically
495 estimate all spike positions and orientations on the viral membranes (71 virions used, ~9,000
496 subtomograms), which were then iteratively refined following PEET guidelines using the previously

497 generated initial reference. Duplicate particles were discounted at each stage. After the initial
498 refinements C3 symmetry was evident, therefore in later stages pseudo-particles representing the 3
499 possible orientations of each tripod were calculated, thereby tripling the number of subtomograms.
500 Additionally, re-creating unbinned tomograms using -30˚ to +30˚ tilt angles, to remove the
501 projections from high tilt angles, improved the resolution achievable in STA. For the whole tripod,
502 this resulted in 20,282 subtomograms with a calculated FSC resolution of ~9.1 Å, using the calcFSC
503 PEET programme and a 0.5 cutoff. The subtomogram average of the floor region was generated as
504 above, but centring the average on this region instead of the tripod (using the modifyMotiveList
505 programme) and then iteratively refining the locations and orientations of the subtomograms. This
506 similarly resulted in 16,096 subtomograms, but an improved resolution of ~6.6 Å (0.5 FSC cutoff) of
507 this region using the full dataset.

508 For accurate structural determination and resolution calculations GS-FSC was also performed on
509 half split datasets. For GS-FSC resolution estimation, all automatically selected particles were
510 passed through an initial iteration to remove duplicate particles. The remaining particles were split
511 into half dataset and independently aligned and averaged following identical steps to that outlined
512 above. The half datasets were then aligned to bring the two averages into a common position and
513 orientation, following PEET guidelines. The FSC between the two half maps was computed using
514 the calcUnbiasedFSC programme (PEET), the result of which was used to filter the resolution of the
515 full dataset. This resulted in an unbiased FSC calculation (using a 0.143 cutoff) for the tripod was
516 ~16 Å and ~14 Å for the floor STA.

517 For the pH 6.3/K^+ treated virus STA, automatic selection of spikes using seedSpikes, did not result
518 in a coherent average. Subtomograms were therefore manually selected (~20,000) from 89 virions
519 and alignment was refined iteratively using the initial reference, obtained as for the control. No
520 symmetry was evident and therefore was not applied. Additionally, the density at the top of the
521 spikes could not be well refined suggesting multiple conformations. To address this, principal
522 components analysis (pca) and clusterPca programmes were used to identify clusters of separate
523 conformations. Three clusters were identified however the top of the spikes remained unresolved for

524 all (this was also the case for all the clustering options explored) and therefore suggested a highly
525 dynamic structure. The largest cluster (9,987 subtomograms) was taken forward for further
526 refinements utilising a loosely fitted mask to improve the more structured regions and resulted in
527 ~16 Å resolution. This was determined using the calcFSC (0.5 cutoff) PEET programme (not GS-
528 FSC), owing to the high flexibility and low resolution of the average.

529 Subtomograms were visualised using Chimera and ChimeraX (52,53). Fitting of the BUNV head
530 domain (pdb: 6H3V), SBV stalk (pdb: 6H3S) (16) and the LACV fusion domains (pre-fusion
531 modelled from pdb: 7A57) was also performed in Chimera X. Comparison of the RMSD values
532 comparing the individual domain structures of the LACV and AlphaFold Gc fusion domains was
533 obtained using the matchmaker command in Chimera X. RMSD values for the pruned atom pairs
534 and all atom pairs were obtained: DI pruned pairs (65 atoms) 1.08 Å and all pairs (122 atoms) 5.83
535 Å; DII pruned pairs (137 atoms) 1.16 Å and all pairs (186 atoms) 1.91 Å; DIII pruned pairs (78
536 atoms) 0.95 Å and all pairs (84 pairs) 1.16 Å.

537 AlphaFold v2.1 was used to generate the multimer structure of the BUNV Gn/Gc complex, using the
538 M segment polyprotein (Gn-NSm-Gc) sequence for Gn and Gc from ncbi (17,27). At the time of
539 model generation, only the Gc head and stalk domains were available for orthobunyaviruses; no Gc
540 fusion domain nor Gn structures were available for training the model. For fitting into the tripod STA,
541 the output model was rotated about the flexible inter-domain regions (which also have low model
542 confidence) head-stalk and stalk sub-domains I-II (see Supplementary Fig. 6c).

543 **Data Availability**

544 The STA structures of the (pH 7.3/no K^+) BUNV tripod (accession number: EMD-15557), floor
545 region (EMD-15569) and pH 6.3/K^+ GPs (EMD-15579) have been deposited in EMBD. The
546 AlphaFold model, lacking the TMDs (which are not supported by the STA data) can be found as
547 Supplementary Material 1. Correspondence of materials: John N. Barr (J.N.Barr@leeds.ac.uk).

Acknowledgements

Thanks to the Astbury Biostructure Laboratory electron microscopy facility for support in using the microscopes, and a particular thanks to Dr Emma Hesketh, Dr Rebecca Thompson and Dr Daniel Maskell (University of Leeds) for the cryo-electron tomography data collection setup. Thanks to Professor Félix Rey (Institut Pasteur, Paris) for kindly providing the structure of the LACV post-fusion Gc prior to publication and for useful comments on the manuscript. Thanks also to Dr Xiaohong Shi, Professor Richard Elliott and Professor Alain Kohl from the Glasgow Centre for Virus Research (CVR, University of Glasgow), and Dr Cheryl Walter (University of Hull) for providing reagents.

Funding

J.F. was funded by the University of Leeds (University Academic Fellow scheme). This work was funded by the Human Frontiers Science Program (RGP0040/2019), the Academy of Medical Sciences and the Wellcome Trust (Springboard Award, SBF002\1029), the Rosetrees Trust (A1618) and the MRC (MR/T016159/1). Electron Microscopy was performed at the Astbury Biostructure Laboratory (University of Leeds), which was funded by the University of Leeds and the Wellcome Trust (108466/Z/15/Z and 090932/Z/09/Z). The IncuCyte ZOOM live imaging system was funded by the BBSRC (BB/P001459/1), awarded to Professor Nicola Stonehouse (University of Leeds).

Ethics Declaration

Competing interests: The authors declare no competing interests.

References

1. Briese T, Calisher CH, Higgs S. Viruses of the family Bunyaviridae: are all available isolates reassortants? Virology. 2013 Nov;446(1–2):207–16.
2. Elliott RM. Emerging viruses: the Bunyaviridae. Mol Med. 1997;3(9):572.
3. Abudurexiti A, Adkins S, Alioto D, Alkhovsky S V., Avšič-Županc T, Ballinger MJ, et al. Taxonomy of the order Bunyavirales: update 2019. Arch Virol. 2019 May 7;1–17.
4. Zeller H, Bouloy M. Infections by viruses of the families Bunyaviridae and Filoviridae. Rev Sci Tech. 2000;19(1):79–91.
5. Huotari J, Helenius A. Endosome maturation. EMBO J. 2011 Aug 31;30(17):3481.

576 6. Harrison SC. Viral membrane fusion. Virology. 2015 May 1;479–480:498–507.

577 7. Halldorsson S, Behrens A-J, Harlos K, Huiskonen JT, Elliott RM, Crispin M, et al. Structure of
578 a phleboviral envelope glycoprotein reveals a consolidated model of membrane fusion. Proc
579 Natl Acad Sci U S A. 2016 Jun 28;113(26):7154–9.

580 8. Acuña R, Bignon EA, Mancini R, Lozach P-Y, Tischler ND. Acidification triggers Andes
581 hantavirus membrane fusion and rearrangement of Gc into a stable post-fusion homotrimer. J
582 Gen Virol. 2015 Nov 1;96(11):3192–7.

583 9. de Boer SM, Kortekaas J, Spel L, Rottier PJM, Moormann RJM, Bosch BJ. Acid-Activated
584 Structural Reorganization of the Rift Valley Fever Virus Gc Fusion Protein. J Virol. 2012 Dec
585 15;86(24):13642–52.

586 10. Hover S, Foster B, Fontana J, Kohl A, Goldstein SAN, Barr JN, et al. Bunyavirus requirement
587 for endosomal K+ reveals new roles of cellular ion channels during infection. PLOS Pathog.
588 2018 Jan 19;14(1):e1006845.

589 11. Hover S, King B, Hall B, Loundras E-A, Taqi H, Daly J, et al. Modulation of potassium
590 channels inhibits bunyavirus infection. J Biol Chem. 2016 Dec 16;291(7):3411–22.

591 12. Charlton FW, Hover S, Fuller J, Hewson R, Fontana J, Barr JN, et al. Cellular cholesterol
592 abundance regulates potassium accumulation within endosomes and is an important
593 determinant in bunyavirus entry. J Biol Chem. 2019 May 3;294(18):7335–47.

594 13. Punch EK, Hover S, Blest HT, Fuller J, Hewson R, Fontana J, et al. Potassium is a trigger for
595 conformational change in the fusion spike of an enveloped RNA virus. J Biol Chem. 2018 Apr
596 20;293(26):9937–44.

597 14. Sandler ZJ, Firpo MR, Omoba OS, Vu MN, Menachery VD, Mounce BC. Novel Ionophores
598 Active against La Crosse Virus Identified through Rapid Antiviral Screening. Antimicrob
599 Agents Chemother. 2020 Jun 1;64(6).

600 15. Windhaber S, Xin Q, Uckeley ZM, Koch J, Obr M, Garnier C, et al. The Orthobunyavirus
601 Germiston Enters Host Cells from Late Endosomes. J Virol. 2022 Mar 9;96(5).

602 16. Hellert J, Aebischer A, Wernike K, Haouz A, Brocchi E, Reiche S, et al. Orthobunyavirus
603 spike architecture and recognition by neutralizing antibodies. Nat Commun. 2019 Dec
604 20;10(1):879.

605 17. Jumper J, Evans R, Pritzel A, Green T, Figurnov M, Ronneberger O, et al. Highly accurate
606 protein structure prediction with AlphaFold. Nature. 2021 Jul 15;596(7873):583–9.

607 18. Stauffer S, Feng Y, Nebioglu F, Heilig R, Picotti P, Helenius A. Stepwise priming by acidic pH
608 and a high K+ concentration is required for efficient uncoating of influenza A virus cores after
609 penetration. J Virol. 2014 Nov;88(22):13029–46.

610 19. Bowden TA, Bitto D, McLees A, Yeromonahos C, Elliott RM, Huiskonen JT. Orthobunyavirus
611 ultrastructure and the curious tripodal glycoprotein spike. PLOS Pathog. 2013;9(5):e1003374.

612 20. Shi X, van Mierlo JT, French A, Elliott RM. Visualizing the replication cycle of bunyamwera
613 orthobunyavirus expressing fluorescent protein-tagged Gc glycoprotein. J Virol.
614 2010;84(17):8460–9.

615 21. Shi X, Goli J, Clark G, Brauburger K, Elliott RM. Functional analysis of the Bunyamwera
616 orthobunyavirus Gc glycoprotein. J Gen Virol. 2009 Oct;90(Pt 10):2483–92.

617 22. Hopkins FR, Álvarez-Rodríguez B, Heath GR, Panayi K, Hover S, Edwards TA, et al. The
618 Native Orthobunyavirus Ribonucleoprotein Possesses a Helical Architecture. Brennan B,
619 Cherry S, editors. MBio. 2022 Jun 28;

620 23. Hulswit RJG, Paesen GC, Bowden TA, Shi X. Recent advances in bunyavirus glycoprotein
621 research: Precursor processing, receptor binding and structure. Vol. 13, Viruses. MDPI AG;
622 2021.

623 24. Dessau M, Modis Y. Crystal structure of glycoprotein C from Rift Valley fever virus. Proc Natl
624 Acad Sci U S A. 2013 Jan 29;110(5):1696–701.

625 25. Guardado-Calvo P, Atkovska K, Jeffers SA, Grau N, Backovic M, Pérez-Vargas J, et al. A
626 glycerophospholipid-specific pocket in the RVFV class II fusion protein drives target
627 membrane insertion. Science (80-). 2017 Nov 3;358(6363):663–7.

628 26. Serris A, Stass R, Bignon EA, Muena NA, Manuguerra J-C, Jangra RK, et al. The Hantavirus
629 Surface Glycoprotein Lattice and Its Fusion Control Mechanism. Cell. 2020 Sep
630 15;183(2):442–56.

631 27. Evans R, O'Neill M, Pritzel A, Antropova N, Senior A, Green T, et al. Protein complex
632 prediction with AlphaFold-Multimer. bioRxiv. 2021 Oct 4;2021.10.04.463034.

633 28. Guardado-Calvo P, Rey FA. The Viral Class II Membrane Fusion Machinery: Divergent
634 Evolution from an Ancestral Heterodimer. Viruses. 2021 Nov 1;13(12).

635 29. Lappin DF, Nakitare GW, Palfreyman JW, Elliott RM. Localization of Bunyamwera bunyavirus
636 G1 glycoprotein to the Golgi requires association with G2 but not with NSm. J Virol. 1994 Dec
637 1;75(Pt 12):3441–51.

638 30. Shi X, Brauburger K, Elliott RM. Role of N-linked glycans on bunyamwera virus glycoproteins
639 in intracellular trafficking, protein folding, and virus infectivity. J Virol. 2005;79(21):13725–34.

640 31. Guardado-Calvo P, Bignon EA, Stettner E, Jeffers SA, Pérez-Vargas J, Pehau-Arnaudet G,
641 et al. Mechanistic Insight into Bunyavirus-Induced Membrane Fusion from Structure-Function
642 Analyses of the Hantavirus Envelope Glycoprotein Gc. Kuhn RJ, editor. PLOS Pathog. 2016
643 Oct 26;12(10):e1005813.

644 32. Halldorsson S, Li S, Li M, Harlos K, Bowden TA, Huiskonen JT. Shielding and activation of a
645 viral membrane fusion protein. Nat Commun. 2018 Dec 24;9(1):349.

646 33. Bitto D, Halldorsson S, Caputo A, Huiskonen JT. Low pH and Anionic Lipid-dependent Fusion
647 of Uukuniemi Phlebovirus to Liposomes. J Biol Chem. 2016 Mar 18;291(12):6412–22.

648 34. Overby A, Pettersson R, Grünewald K, Huiskonen J. Insights into bunyavirus architecture
649 from electron cryotomography of Uukuniemi virus. Proc Natl Acad Sci U S A. 2008 Feb
650 19;105(7):2375–9.

651 35. Freiberg A, Sherman M, Morais M, Holbrook M, Watowich S. Three-dimensional organization
652 of Rift Valley fever virus revealed by cryoelectron tomography. J Virol. 2008 Nov
653 1;82(21):10341–8.

654 36. Sherman M, Freiberg A, Holbrook M, Watowich S. Single-particle cryo-electron microscopy of
655 Rift Valley fever virus. Virology. 2009 Apr 25;387(1):11–5.

656 37. Huiskonen J, Overby A, Weber F, Grünewald K. Electron cryo-microscopy and single-particle
657 averaging of Rift Valley fever virus: evidence for GN-GC glycoprotein heterodimers. J Virol.
658 2009 Apr 15;83(8):3762–9.

659 38. Voss JE, Vaney MC, Duquerroy S, Vonrhein C, Girard-Blanc C, Crublet E, et al. Glycoprotein
660 organization of Chikungunya virus particles revealed by X-ray crystallography. Nature. 2010
661 Dec 2;468(7324):709–12.

662 39. Guardado-Calvo P, Rey FA. The Envelope Proteins of the Bunyavirales. Adv Virus Res. 2017
663 Jan 1;98:83–118.

664 40. Guardado-Calvo P, Rey FA. The surface glycoproteins of hantaviruses. Vol. 50, Current
665 Opinion in Virology. Elsevier; 2021. p. 87–94.

666 41. Bignon EA, Albornoz A, Guardado-Calvo P, Rey FA, Tischler ND. Molecular organization and
667 dynamics of the fusion protein Gc at the hantavirus surface. Elife. 2019 Jun 10;8:e46028.

668 42. Rissanen I, Stass R, Zeltina A, Li S, Hepojoki J, Harlos K, et al. Structural transitions of the

conserved and metastable hantaviral glycoprotein envelope. J Virol. 2017;91(21):378–417.

43. Hofmann H, Li X, Zhang X, Liu W, Kuhl A, Kaup F, et al. Severe Fever with Thrombocytopenia Virus Glycoproteins Are Targeted by Neutralizing Antibodies and Can Use DC-SIGN as a Receptor for pH-Dependent Entry into Human and Animal Cell Lines. J Virol. 2013 Apr 15;87(8):4384–94.

44. Sabella E, Pierro R, Panattoni A, Materazzi A, Vergine M, De Bellis L, et al. Effects of modulation of potassium channels in tobacco mosaic virus elimination. Physiol Mol Plant Pathol. 2018 Apr 1;102:180–4.

45. Pearson H, Todd EJAA, Ahrends M, Hover SE, Whitehouse A, Stacey M, et al. TMEM16A/ANO1 calcium-activated chloride channel as a novel target for the treatment of human respiratory syncytial virus infection. Thorax. 2021 Jan 1;76(1):64–72.

46. Hopkins FR, Álvarez-Rodrígues B, Heath GR, Panayi K, Hover S, Edwards TA, et al. The structure of a native orthobunyavirus ribonucleoprotein reveals a key role for viral RNA in maintaining its helical architecture. bioRxiv. 2021;

47. Zhang K. Gctf: Real-time CTF determination and correction. J Struct Biol. 2016 Jan 1;193(1):1–12.

48. Xiong Q, Morphew MK, Schwartz CL, Hoenger AH, Mastronarde DN. CTF determination and correction for low dose tomographic tilt series. J Struct Biol. 2009 Dec;168(3):378–87.

49. Mastronarde DN, Held SR. Automated tilt series alignment and tomographic reconstruction in IMOD. J Struct Biol. 2017 Feb 1;197(2):102–13.

50. Nicastro D, Schwartz CL, Pierson J, Gaudette R, Porter ME, Richard MJ. The molecular architecture of axonemes revealed by cryoelectron tomography. Science (80-). 2006 Aug 18;313(5789):944–8.

51. Heymann JB, Belnap DM. Bsoft: image processing and molecular modeling for electron microscopy. J Struct Biol. 2007 Jan;157(1):3–18.

52. Pettersen EF, Goddard TD, Huang CC, Couch GS, Greenblatt DM, Meng EC, et al. UCSF Chimera--a visualization system for exploratory research and analysis. J Comput Chem. 2004 Oct;25(13):1605–12.

53. Pettersen EF, Goddard TD, Huang CC, Meng EC, Couch GS, Croll TI, et al. UCSF ChimeraX: Structure visualization for researchers, educators, and developers. Protein Sci. 2021 Jan 1;30(1):70–82.

54. Scott CCC, Gruenberg J. Ion flux and the function of endosomes and lysosomes: pH is just the start. Bioessays. 2011 Feb;33(2):103–10.

Figures

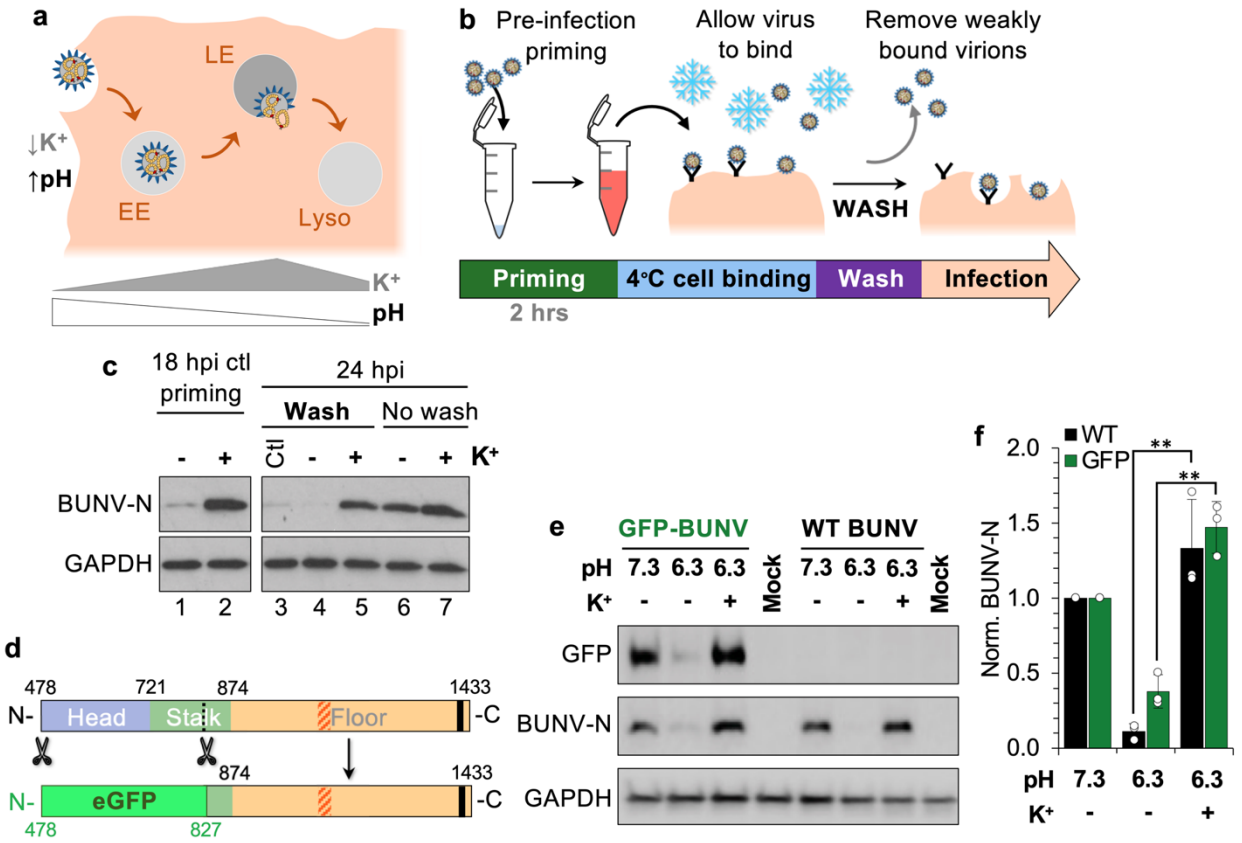

Fig. 1 Mimicking endosomal pH and K^+ in vitro expedites BUNV entry by altering the BUNV GPs. **a** Schematic of the endocytic pathway. The extracellular environment presents a neutral pH (~7.3) and low [K^+] (~5 mM). Alongside the canonical decrease in pH during endosome maturation, the [K^+] increases with passage through early endosomes (EE) peaking in late endosome (LE), and is lower within lysosomes (Lyso). The [K^+] is high in the cytoplasm (~150 mM). (10,54). **b** Workflow of the binding assay, whereby BUNV virions are pre-infection treated for 2 hrs pre-infection with pH 7.3/no K^+ (Ctl), pH 6.3/no K^+ or pH 6.3/K^+ buffers (as previously described (10)). Buffer is diluted out and then virions are bound to cells at 4 ˚C. Weakly or unbound virions are removed by three PBS washes; or a no wash control. Infection is allowed to proceed for 18 hrs (internal control) or 24 hrs, then cells are lysed and **c** western blot analysed using antibodies against BUNV-N (a known marker of infection) or GAPDH (loading control). **d** Schematic of WT versus eGFP-tagged BUNV Gc protein (GFP-BUNV), with the removed section of the Gc head/stalk domains indicated, which were replaced with eGFP (20). **e** WT and GFP-BUNV were treated with pH 7.3/no K^+, pH 6.3/no K^+ or pH 6.3/K^+, and infection (or non-infected, mock) was assessed by western blot at 18 hpi. **f** Densitometry of n=3 western blots from *d* normalised to each loading control and then to the pH 7.3/no K^+ control (individual data points shown as white spheres). Error bars indicate mean ± standard error (SE), and significant difference ** = $P<0.005$ observed between the reduction at pH 6.3/no K^+ and the recovery at pH 6.3/K^+.

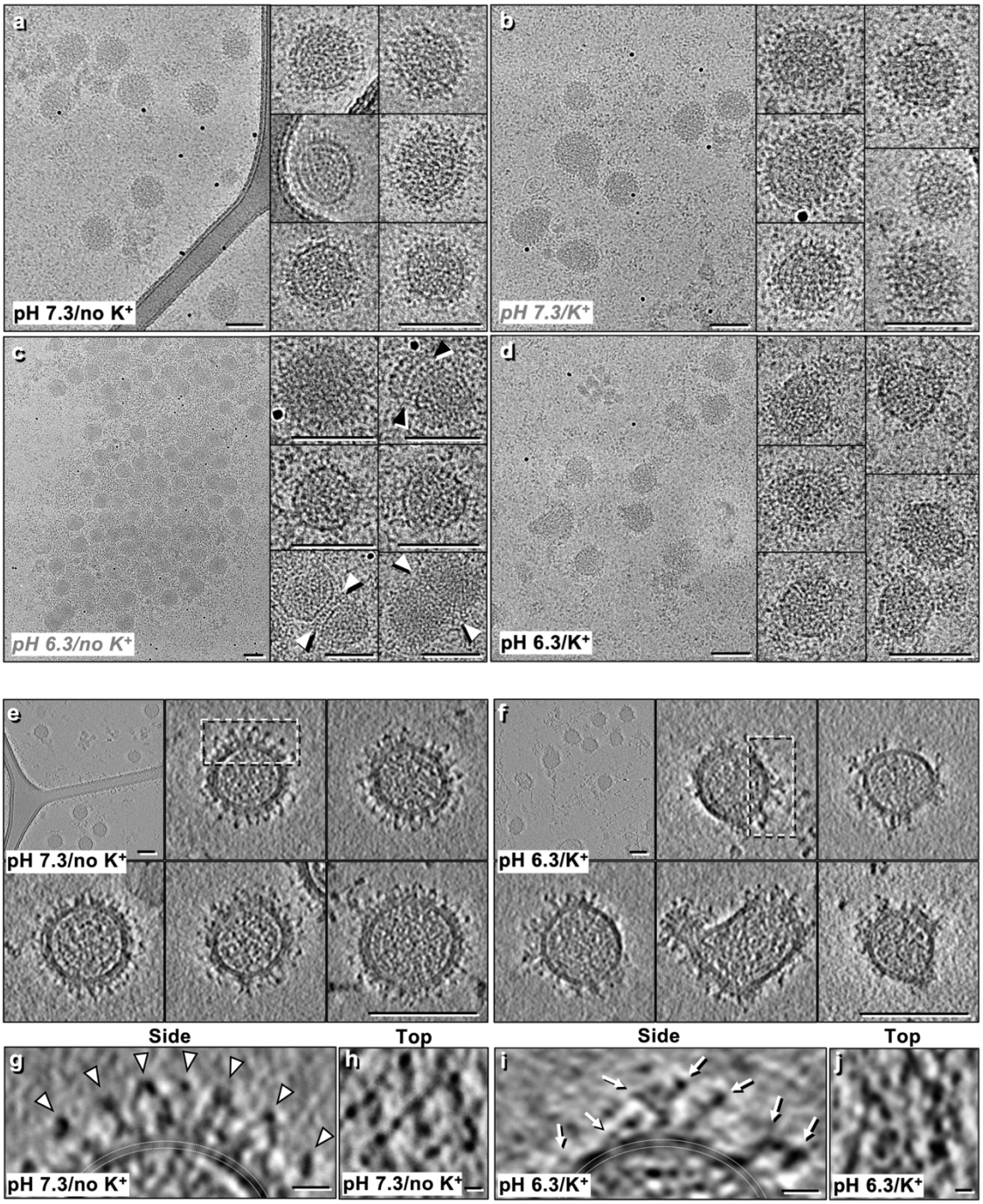

Fig. 2 pH 6.3/K^+ disrupts the BUNV GP spike arrangements on the virion surface. Cryo-EM micrographs of BUNV virions treated under different conditions prior to plunge freezing: **a** pH 7.3/no K^+, **b** pH 7.3/K^+, **c** pH 6.3/no K^+ and **d** pH 6.3/K^+. White arrowheads in *c* indicate flattened virion contacts with one another and black arrowheads indicate curved membrane contacts. **e-j** Cryo-ET tilt series were collected of pH 7.3/no K^+ and pH 6.3/K^+ treated virions, then 3D tomographic reconstructions were calculated. **e** Slices through tomograms of pH 7.3/no K^+ treated virions (control). **f** As in *e*, with pH 6.3/K^+ treated virions which show clear disruption to the regular arrangement of GPs. **g,h** Slice through the side (from the white dashed box in *e*) and top of a pH 7.3/no K^+ treated virion. White arrows indicate tripodal arrangement and triangles in *h* emphasise the trimeric architecture and local lattice. **i,j** As in *g,h*, however from pH 6.3/K^+ virions where side (from box in *f*) and top views show a disruption to the GP tripods and the local lattice. White arrows indicate spike 'ends' that no longer appear connected in tripods. Scale bars: *a-f* = 100 nm; *g-j* = 10 nm.

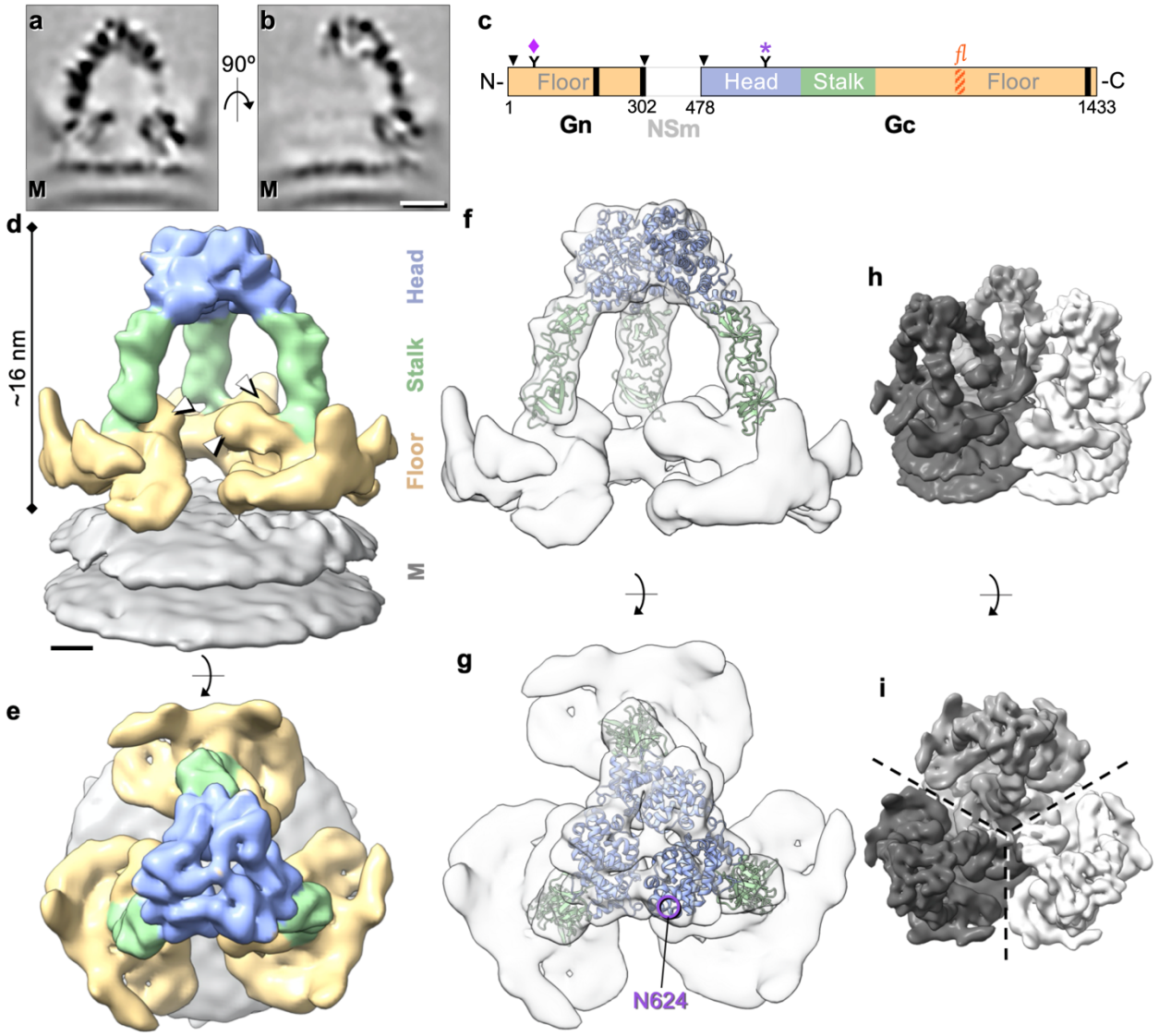

Fig. 3 BUNV GPs exhibit a trimeric tripod-like architecture. STA of over 20,000 GP spikes aligned through iterative refinements, generating a ~16 Å average (GS-FSC) (EMD-15557). **a,b** Sections through the electron density averages, showing a trimeric spike on top of the viral lipid bilayer (M; membrane). **c** Schematic of the M segment polyprotein constituted by Gn, NSm and Gc. The Gc protein is comprised of three sections: the head, stalk and floor regions. The fusion loop (*fl*; orange striped) resides in the floor region. Arrowheads indicate cleavage sites, black bars the predicted TMDs, numbers the amino acid residues, and 'Y' the glycans N60 (Gn, ♦) and N624 (Gc, ∗, mAb-742 binding epitope) (16,21,29,30). **d,e** Isosurface rendering of the GP trimer, identifying the three regions; head (light blue), stalk (light green) and floor (gold; where Gn also resides) on top of the viral membrane (grey). White arrowheads indicate a previously unresolved region in the floor. **f,g** The previously solved X-ray structures of the BUNV head (pdb: 6H3V; light blue) and SBV stalk (pdb: 6H3S; light green) domains were fitted into our model (16). The glycosylation site N624 is indicated (purple circle). **h,i** A model of the local lattice arrangement of BUNV GPs, emphasising the two C3 symmetry axes; one forming a tripod, and one in the floor region where three neighbouring tripods connect. Scale bars: *a*, *b* = 5 nm; *d*, *e* = 2 nm.

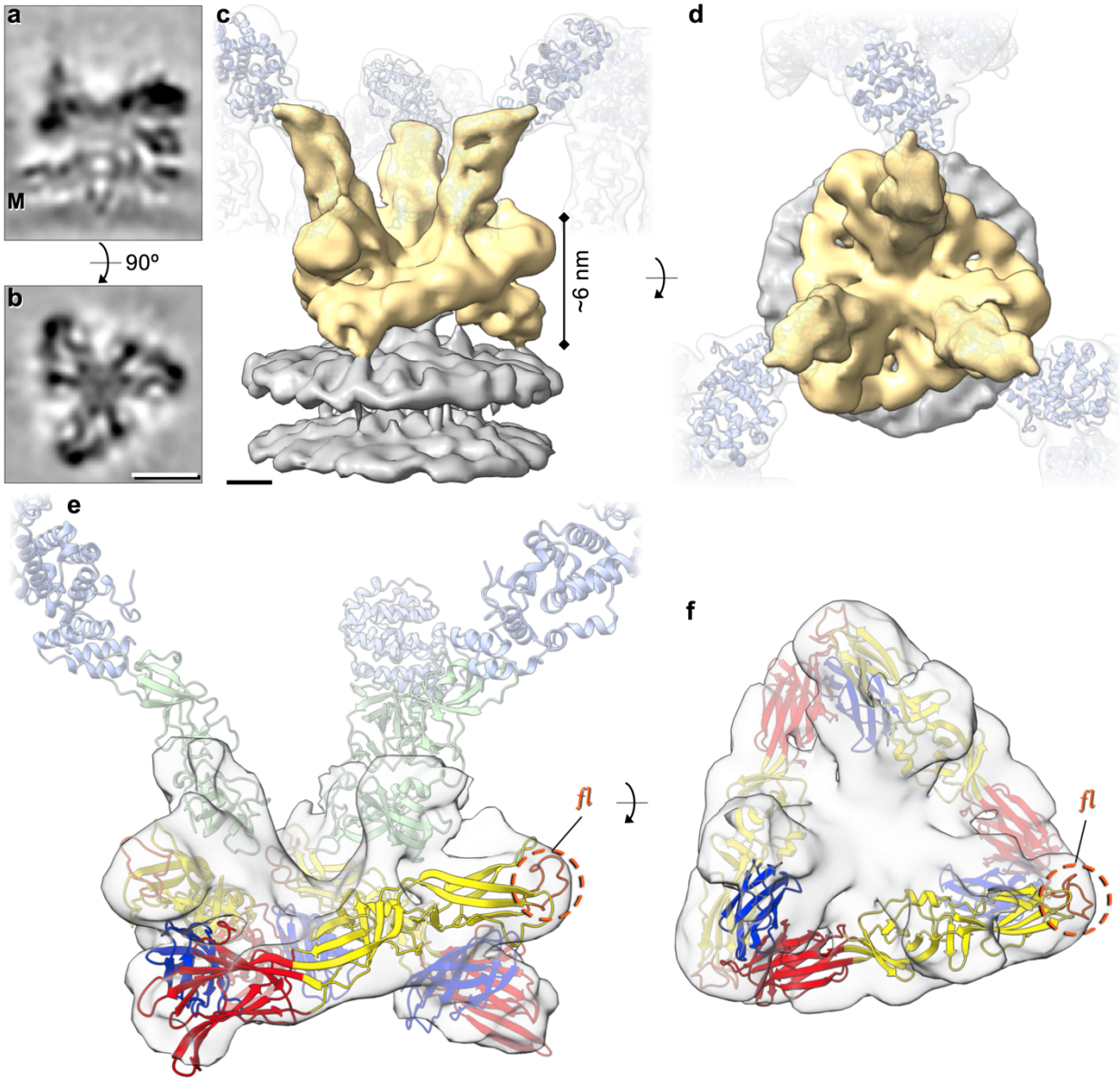

Fig. 4 STA of the floor region allows modelling of the BUNV fusion domain. STA was performed as in *Fig. 3*, however aligning the floor region trimer (as opposed to the tripod). Over 16,000 subtomograms were resolved at ~14 Å resolution (GS-FSC). **a,b** Sections through the electron density of the floor region average atop the viral membrane (M). **c,d** Isosurface rendering of the electron density (*c* side view, *d* top view) of the floor region (gold) atop the viral membrane (grey). Translucent tripods of the head-stalk regions have been added for orientation. **e,f** Modelling of the LACV fusion domain (residues 949-1344; domain I red, domain II yellow, domain III blue) in C3 symmetry within the BUNV floor region (EMD-15569), revealing the location of the fusion loops (*fl*; orange) (post-fusion structure pdb: 7A57). The location of the head (light blue) and stalk (light green) domains are indicated in *e* for orientation. Scale bars: *a*, *b* = 5 nm; c, *d* = 2 nm.

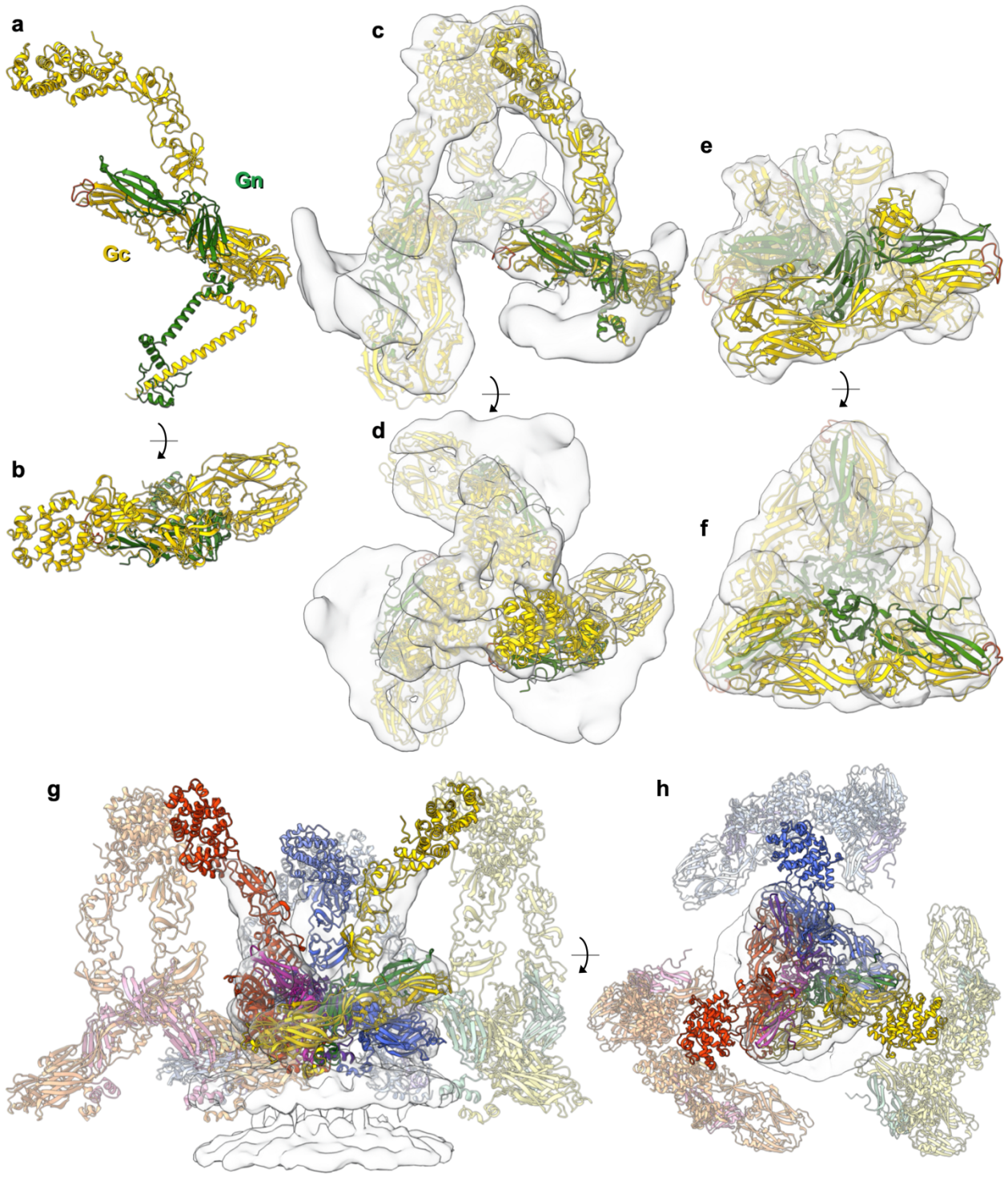

764

765 **Fig. 5** AlphaFold generates a dimeric structure of BUNV Gn and Gc which fits reliably within our GP
766 STA. **a,b** AlphaFold generated an atomic model of the full-length Gn-Gc dimer. Gc in yellow, Gn in
767 green. **c,d** With only minor rotations about the inter-domain regions (*Supplementary Fig. 6c*), this
768 model fitted well within the tripod STA (from *Fig. 3*; AlphaFold pdb found in *Supplementary Material*
769 *1*) in C3 symmetry (Gn-Gc ectodomains are shown; residues Gn 1-187, Gc 1-899; no TMD). **e,f** The
770 Gn ectodomain and the Gc fusion domain with the stalk subdomain II (residues 351-899)
771 additionally fitted well within the floor region STA (from *Fig. 4*) in C3 symmetry. **g,h** A model of the
772 BUNV GP envelope can be predicted, here showing three hetero-hexamers fitted within a floor STA.
773 The Gn-Gc pairings are colour coded as follow; hexamer 1 purple-blue, hexamer 2 green-yellow,
774 hexamer 3 pink-red. *Supplementary Movie 2* also demonstrates this envelope model.

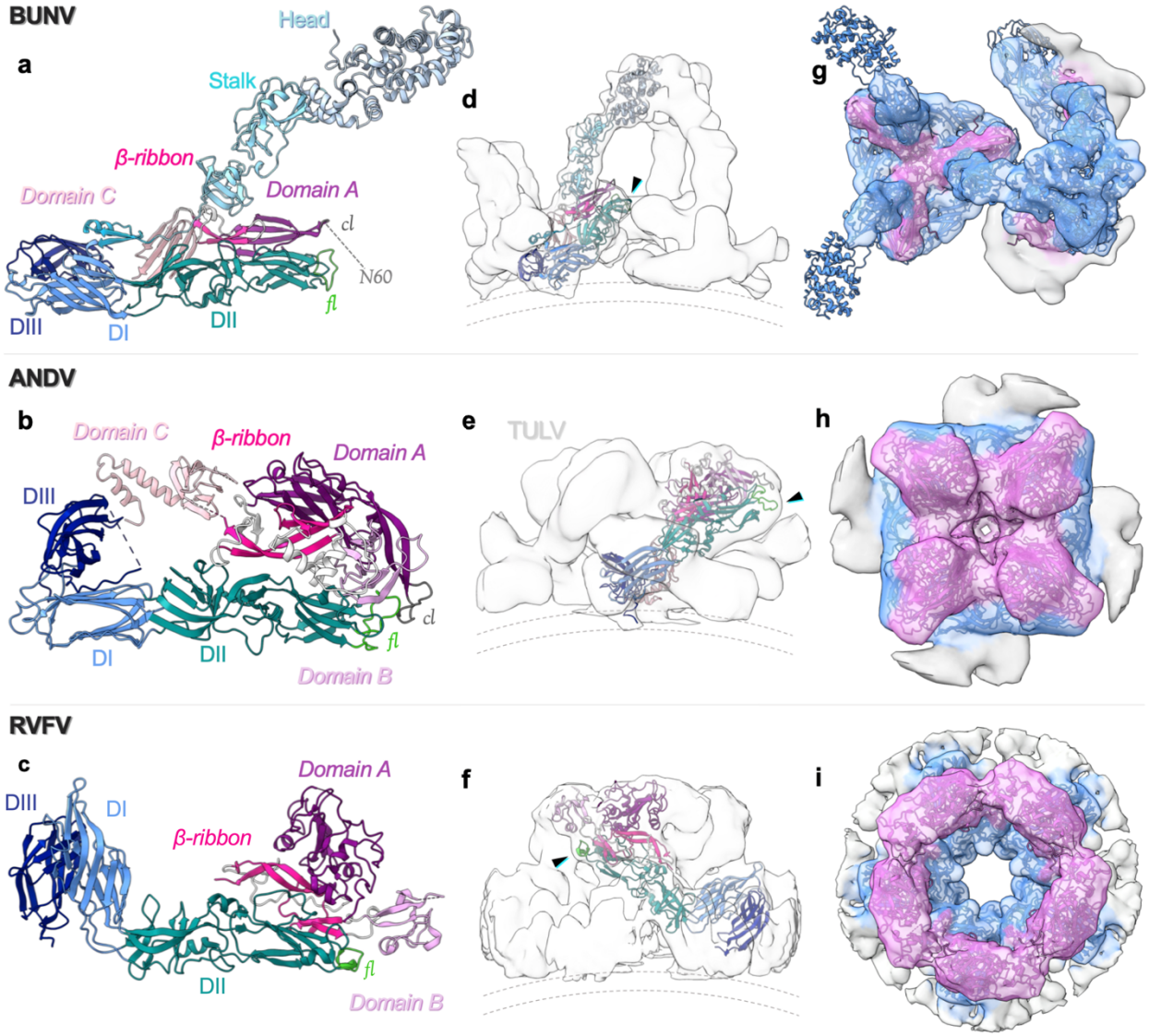

775

776 **Fig. 6** Comparison of GP arrangements of BUNV with that of hantaviruses and phenuiviruses. **a** The
777 BUNV (orthobunyavirus) AlphaFold structure (as in *Fig. 5*) of Gc (shades of blue) and Gn (shades of
778 pink), as compared with the X-ray crystal structures of **b** the hantavirus ANDV (pdb: 6zjm) and **c** the
779 phenuivirus RVFV (in the conformation as fitted within the EM average; pdb: 6f9f). The individual
780 domain colours are correlated between the three models, corresponding to the sub-domains of Gc
781 (head, stalk, domain I (DI), DII, DIII and the fusion loop (*fl*)) and Gn (Domain A, Domain B, Domain
782 C, β-ribbon and the capping loop (*cl*)); as previously described (23,28). The *fl* is shown in green and
783 the *cl* in dark grey for each. **d,e,f** Fit of a single Gn-Gc dimer within the corresponding EM density
784 average; side view. The black arrows indicate the position of the fusion loop and dotted lines the
785 viral membrane. **d** Shows the BUNV AlphaFold fit within the floor and tripod STA (as in *Fig. 5*). **e**
786 ANDV Gn-Gc dimer within TULV STA reconstruction (emd-11236) (26). **f** RVFV Gn-Gc dimer within
787 the EM single-particle reconstruction (emd-4201) (32). **g,h,i** Top-down view of the EM density
788 averages with fitting of the Gn-Gc multimers: **g** BUNV trimer (within the floor and the tripod), **h**
789 ANDV tetramer, **i** RVFV pentamer. The density for each has been coloured by distance from
790 residues of Gn (pink) or Gc (blue), demonstrating the relative positions of each within the complex.

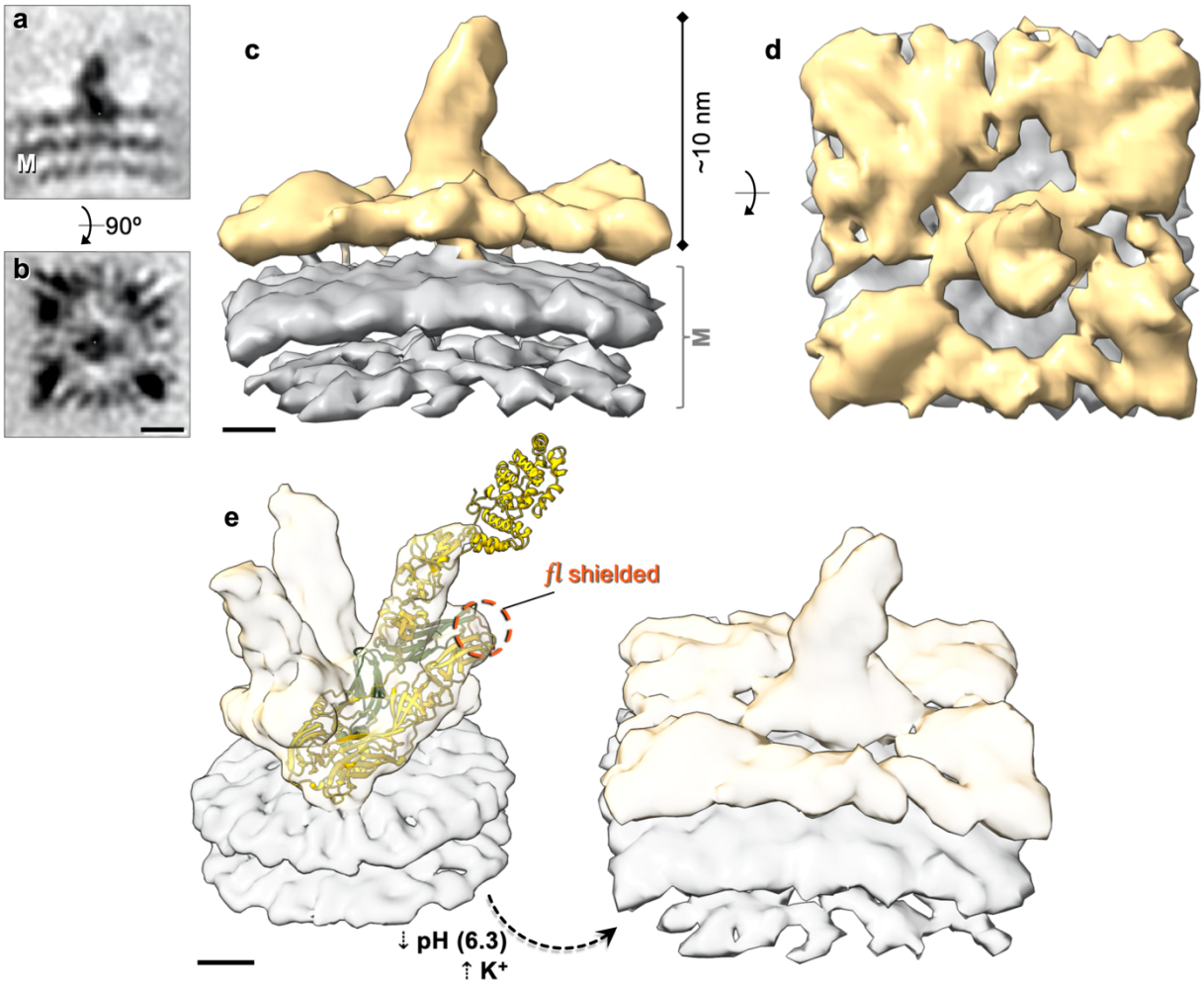

Fig. 7 The trimeric architecture of BUNV GPs is abolished by pH 6.3/K^+ treatment. STA of ~10,000 subtomograms manually selected from the surface of pH 6.3/K^+ virions (EMD-15579). **a,b** Slices through the centre of the spike electron density from the side (*a*) and top (*b*). The viral membrane is indicated (M). **c,d** Isosurface rendering of the density in *a,b*, with the spike (gold) on top of the viral membrane (grey). **e** Scaled comparison of the pH 7.3/no K^+ floor region STA with the AlphaFold model fitted, and the pH 6.3/K^+ STA. The location of the fusion loop (*fl*, orange) is indicated in the pH 7.3/no K^+ floor STA. Scale bars: *a*, *b* = 5 nm; *c*, *d*, *e* = 2 nm.

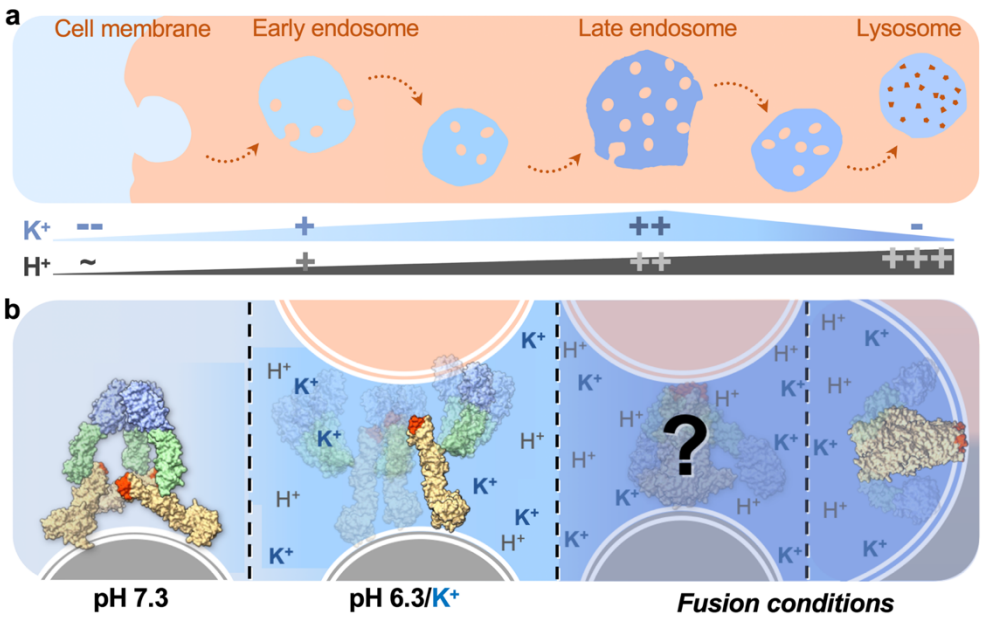

Fig. 8 Proposed stages in BUNV fusion during endocytic entry. **a** Model of endocytic transit; from the cell membrane, through early and late endosomes, and into lysosomes. Canonically pH decreases from pH ~7 to pH ~4, whereas [K^+] is low in the extracellular media and increases with passage into late endosomes, after which decreases again within lysosomes (10,54). **b** BUNV GPs are tripodal and interconnected when entering the cell. During transit, the reducing pH and increasing [K^+] environment acts as a partial trigger, allowing the tripods to uncouple and exposing the fusion loops. Insertion of fusion loops into host membranes alongside an unknown host factor, and potentially a further reduction in pH, cues subsequent intermediate stages yet to be characterised. This is followed by the canonical fold-back of the fusion domains required to pull the viral and host membranes together (23), resulting in the post-fusion conformation similar to that observed for LACV (pdb:7A57).

811 **Supporting Figure Legends**

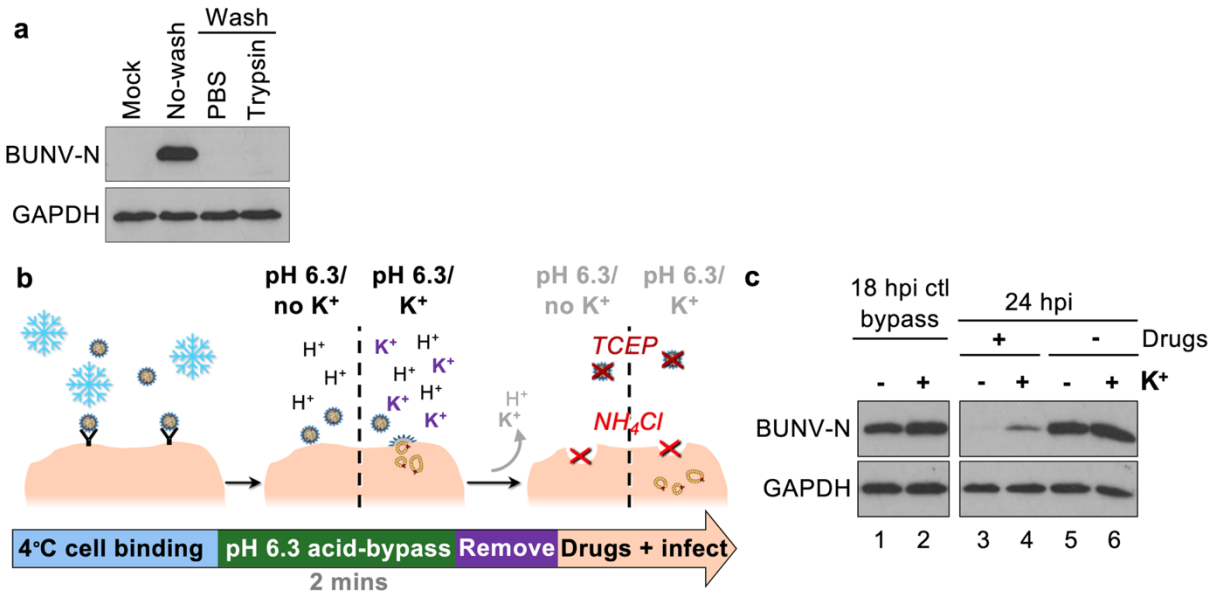

812

813 **Supplementary Fig. 1** pH 6.3/K^+ treatment of BUNV increases interactions with host cells. **a** Virions
814 were bound to cells at 4 ˚C and then weakly bound or unbound virions were removed with three
815 PBS or 0.1x trypsin washes (or no-wash as a control). Cells were warmed to 37 ˚C and infected (or
816 non-infected, mock) for 24 hrs. Western blot analysis of cell lysates (as in *Fig. 1*) using anti-BUNV-N
817 antibodies revealed lack of N signal in the washed samples indicated virions had been removed
818 from the cell membrane. **b** Workflow of an acid-bypass assay. Virions are bound to cells at 4 ˚C and
819 fusion at the plasma membrane is attempted by acid-bypass at pH 6.3/no K^+ (-) or pH 6.3/K^+ (+) for
820 2 mins. Bypass buffer is replaced with media with or without drugs to prevent endocytic entry (TCEP
821 and NH_4Cl). Cells are lysed at 18 hpi (internal control) or 24 hpi and BUNV-N assessed by western
822 blot. **c** Western blot of experiment in *b*, where a BUNV-N signal in the presence of drugs (lanes 3-4)
823 indicates conditions where virions were able to fuse with the plasma membrane.

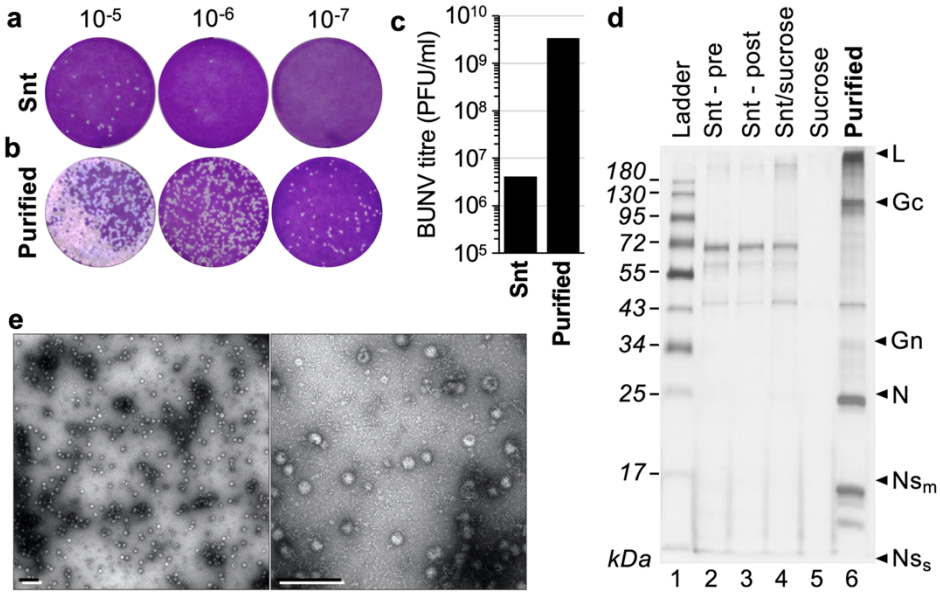

Supplementary Fig. 2 WT BUNV purification. BHK-21 cells were infected with BUNV for 44 hrs and then viral supernatants (snt) were collected and purified by pelleting through a 30% sucrose cushion. Virus was resuspended in 0.1x PBS (Purified) and **a,b,c** the titre was determined by plaque assay as plaque forming units per ml (PFU/ml). **d** SDS-PAGE followed by silver staining of purified BUNV alongside samples collected at each stage of purification; pre-ultracentrifugation supernatant (Snt – pre), post-ultracentrifugation supernatant (Snt – post), supernatant-sucrose cushion interface (Snt/sucrose), and sucrose cushion (Sucrose). The protein ladder sizes are indicated (kDa), as well as the predicted migration of each viral protein based on molecular weight. **e** Negative stain EM of purified BUNV loaded onto carbon coated EM grids and stained with 1% uranyl acetate. Scale bars = 500 nm.

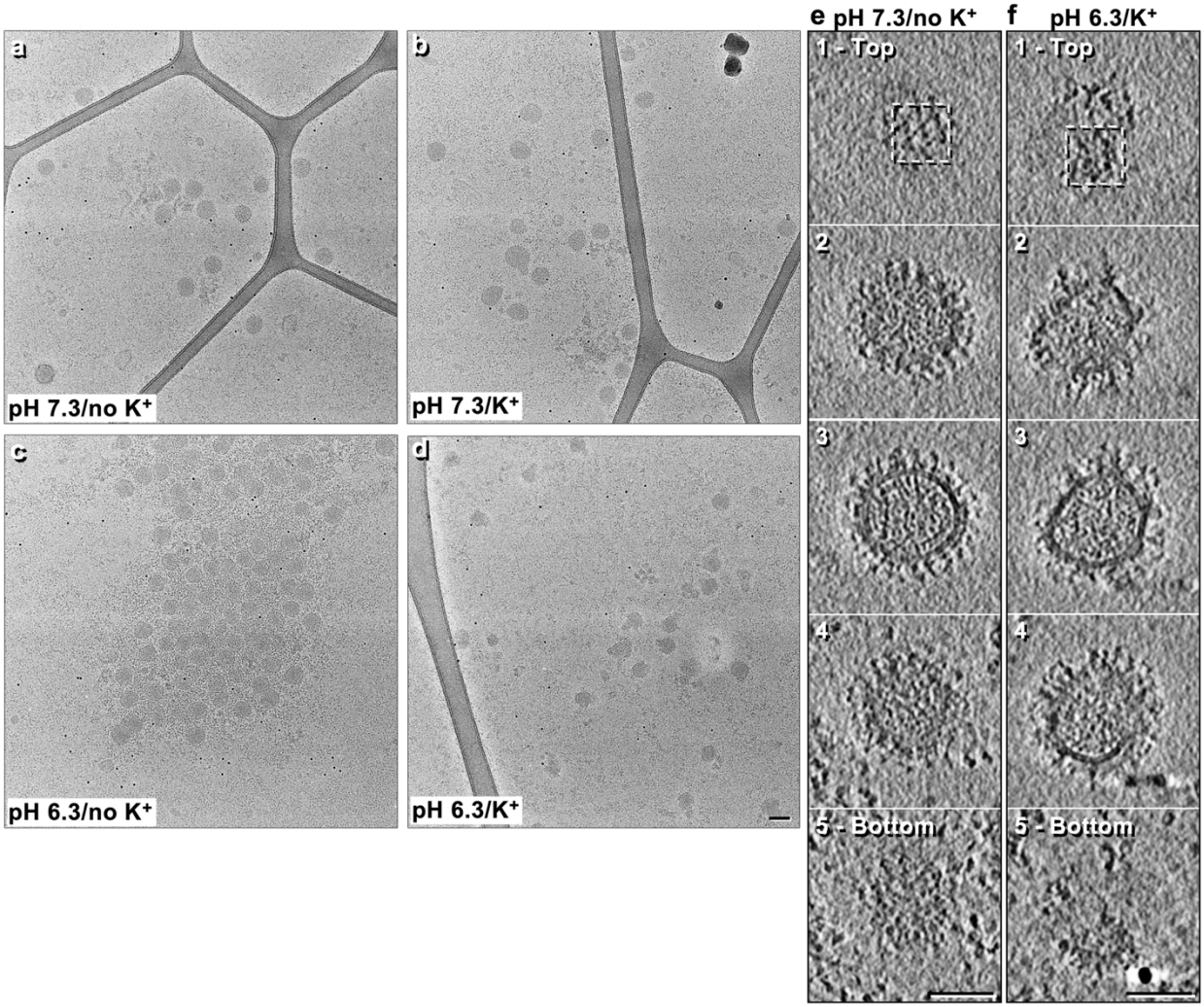

Supplementary Fig. 3 Cryo-EM of BUNV virions under different pH and K^+ conditions. Widefield micrographs of images shown in *Fig. 2*. **a** pH 7.3/no K^+, **b** pH 7.3/K^+, **c** pH 6.3/no K^+ and **d** pH 6.3/K^+ treated virions. **e,f** Slices through the z plane of the cryo-ET (as in *Fig. 2e-j*) of individual pH 7.3/no K^+ (*e*) and pH 6.3/K^+ (*f*) virions. Scale bars = 100 nm.

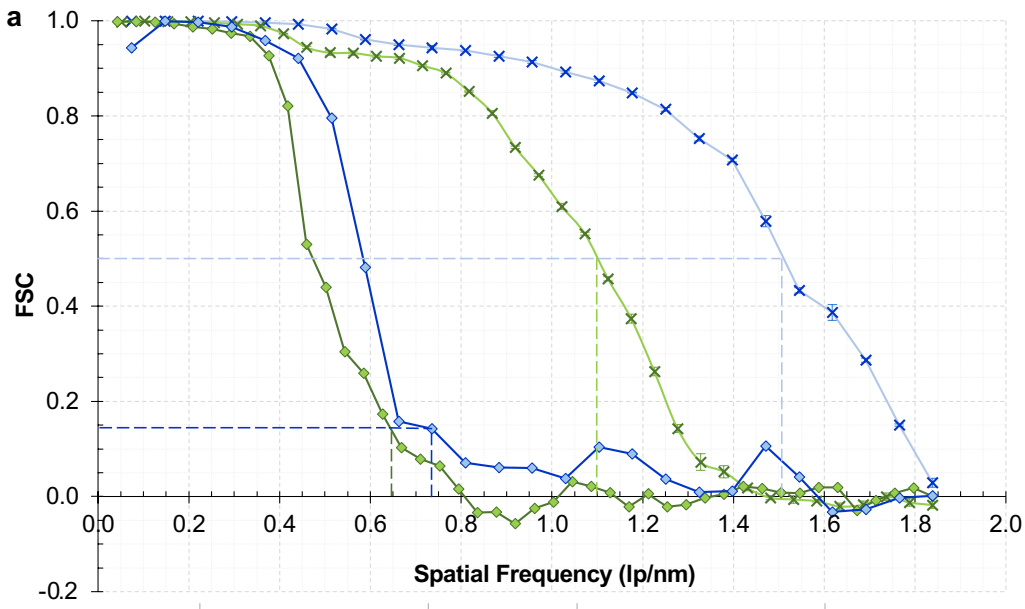

	FSC Calculation	FSC Cutoff	Spatial Freq (lp/nm)	Resolution (Å)
Tripod	Split UnbiasedFSC	0.143	0.65	15.5
	Full Dataset FSC	0.5	1.1	9.1
Floor	Split UnbiasedFSC	0.143	0.74	13.6
	Full Dataset FSC	0.5	1.51	6.6

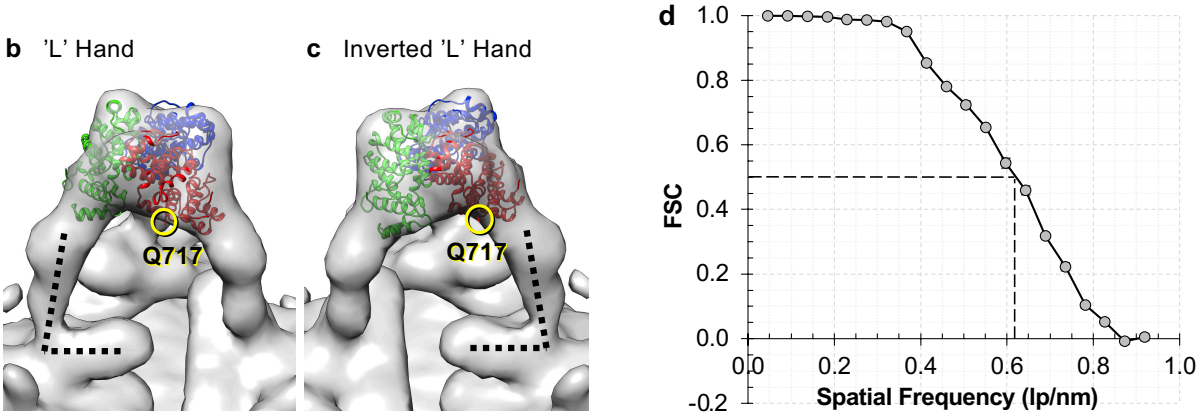

Supplementary Fig. 4 Further analysis of the BUNV GP STA. **a** Fourier shell correlation (FSC) resolution curves of the pH 7.3/no K^+ BUNV tripod (green) and floor (blue) STAs (*Figs. 3,4*). Gold-standard FSC (GS-FSC) calculations (♦ points) were performed by comparing the resolution of half datasets, using a 0.143 FSC cutoff to determine the resolution of each. Standard FSC calculations (× points) were additionally performed to determine the resolution of full datasets using a 0.5 cutoff. Error bars represent standard deviation from the average of n=3 FSC calculations with different pseudo-random assortment of particles into 'half sets' using PEET. **b,c** Fit of the BUNV head domain trimer when switching the handedness; *b* 'L' hand, *c* inverted 'L' hand. Q717 is the C-terminal residue of the head domain which connects to the stalk domain, and is more favourably localised in the inverted 'L' hand (*c*). **d** Standard FSC resolution curve of the pH 6.3/K^+ BUNV STA. The resolution is ~16 Å (*Fig. 7*), using a 0.5 cutoff (used owing to the flexibility of the structure).

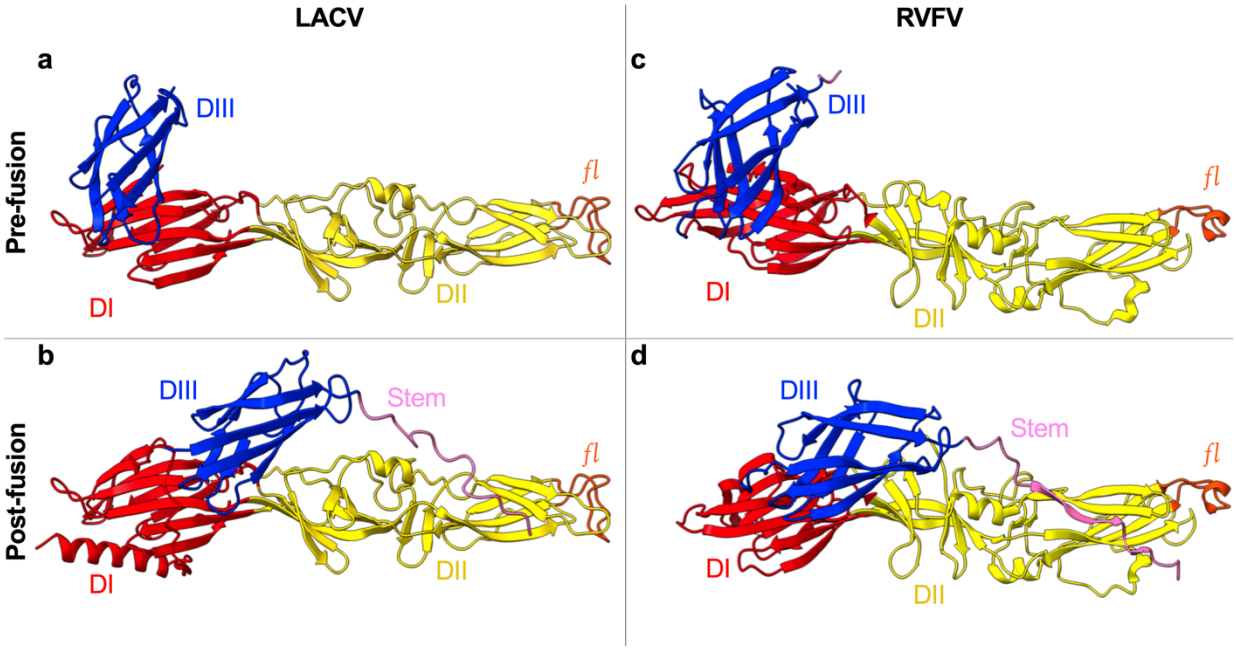

852

853 **Supplementary Fig. 5** Comparison of the LACV and RVFV pre-fusion versus post-fusion class II
854 fusion domain conformations. A monomer of each conformation is represented, where Domain I (DI)
855 is in red, domain II (DII) yellow, domain III (DIII) in blue, the fusion loop (*fl*) in DII is in orange, and
856 the stem region (connecting to the TMD) is in pink. The **a** LACV pre-fusion fusion domain structure
857 (residues 965-1344) is modelled from the **b** post-fusion LACV fusion domain structure (residues
858 928-1364; pdb: 7A57). DIII in *a* has been rotated from its position in *b*, based upon the canonical
859 shift in DIII observed for class II fusion proteins in pre-fusion versus post-fusion conformations.
860 RVFV is shown to exemplify the known shift in DIII during fusion events. RVFV fusion domain also
861 forms a class II fold and structures have been solved for both the **c** pre-fusion (residues 688-1118;
862 pdb: 4HJ1 (24)) and **d** post-fusion conformations (residues 691-1136; pdb: 6EGU (25)). The RVFV
863 pre-fusion conformation (*c*) is represented as in the X-ray structure when Gc is expressed
864 recombinantly outside the context of a virus (*Fig. 6c* represents RVFV Gc flexibility fitted within the
865 EM average of the virus (32)).

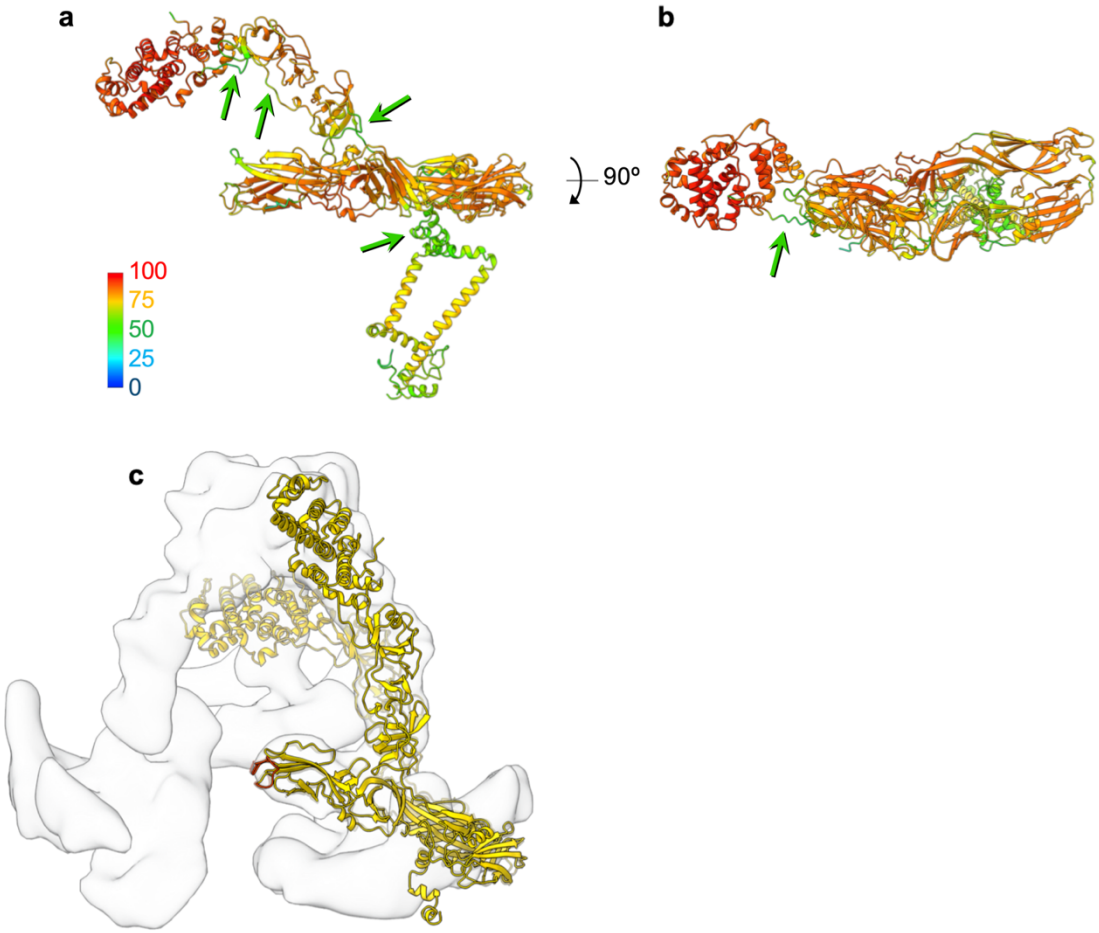

Supplementary Fig. 6 AlphaFold modelling of BUNV Gn-Gc reveals the arrangement of the orthobunyavirus GP envelope. **a,b** The BUNV Gn-Gc model generated by AlphaFold, as in *Fig. 5a,b*, coloured by the per-residue confidence score from 1-100 pLDDT. The majority of residues have a confidence >70 (yellow), indicating the residues were modelled well. Residues >90 are expected to be modelled to high accuracy (17). Key linker-regions have lower confidence (<50) suggesting flexibility between domains compared to the generated model (green arrows). **c** Comparison of the positions of the head and stalk domains in the generated AlphaFold model (translucent), with the fitted model rotated about the head-stalk and stalk sub-domain I-II interfaces.

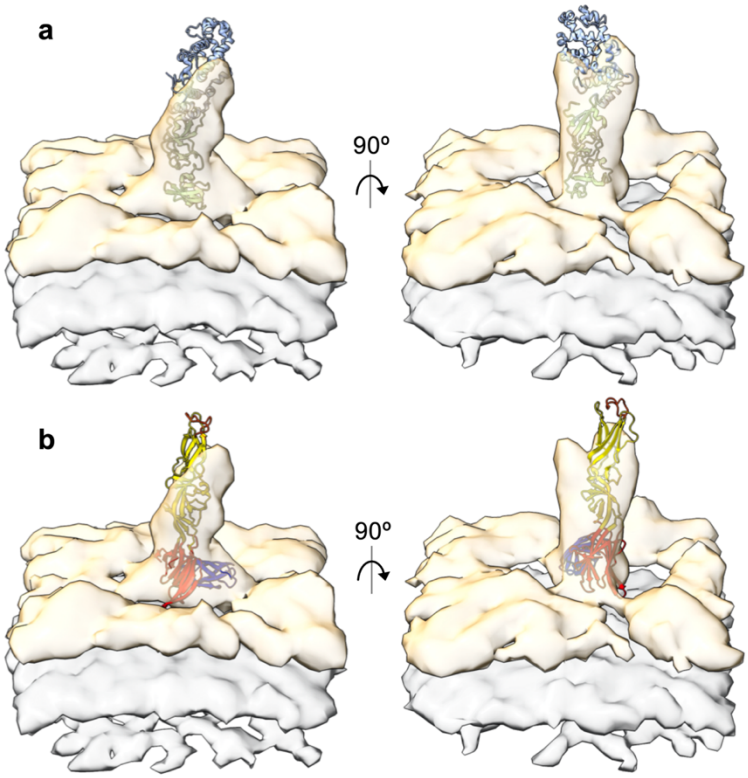

875

876 **Supplementary Fig. 7** Fitting of solved orthobunyavirus Gc crystal structures on the pH 6.3/K^+
877 BUNV STA spike. **a** The BUNV head (light blue, pdb: 6H3V) and SBV stalk (light green, pdb: 6H3S)
878 domains fitted into the spike density. **b** The LACV fusion domain (domains I-III coloured as in
879 *Supplementary Fig. 4*) rotated perpendicular to the viral membrane (grey). DIII (dark blue) remains
880 in proximity to the viral membrane (DIII connects to the C-terminal TMD), with the fusion loops
881 (orange) extending away from the virus.

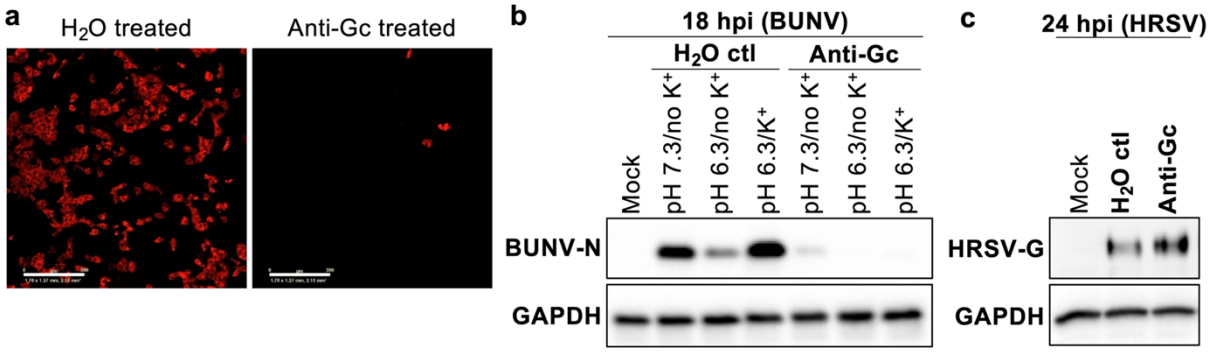

Supplementary Fig. 8 Biochemical characterisation of the Gc head domain after pH 6.3/K^+ treatment. **a** BUNV virions were treated with dH_2O (control) or an anti-Gc neutralising antibody that binds the Gc head domain (mAb-742 (29)) for 1 hr. Virus was then added to A549 cells and incubated for 18 hrs, after which cells were fixed, permeabilised and stained for anti BUNV-N with Alexa-Fluor-594 secondary antibodies. Fluorescence images were acquired using an IncuCyte Zoom, identifying fluorescent infected cells. **b** BUNV was pre-infection treated ('primed'; as in *Fig. 1*), with pH 7.3/no K^+, pH 6.3/no K^+ (controls) or pH 6.3/K^+. Buffer was diluted out and virions neutralised with anti-Gc or a dH_2O control, and A549 cells infected as in *a*. An uninfected control, mock, was also included. Western blot analysis was performed as in *Fig. 1* using anti-BUNV-N and anti-GAPDH (loading control) antibodies. **c** As a control, HRSV was 'neutralised' with anti-Gc or dH_2O as in *a* and infection was assessed at 24 hpi using an anti-HRSV antibody, to confirm antibody specificity.

Supporting Movie Legends

Supplementary Movie 1 Fit of available orthobunyavirus partial-Gc structures and of the BUNV Gn-Gc AlphaFold model within the tripod and floor STA. The BUNV head (6H3V), SBV stalk (6H3S) and LACV fusion domain are fitted as in *Figs. 3,4*; and the BUNV AlphaFold as in *Fig. 5*. CL = capping loop on Gn, FL = fusion loop on Gc. The floor STA is also compared with the pH 6.3/K^+ virus 'spike' as in *Fig 7e*.

Supplementary Movie 2 Modelling the BUNV envelope. An AlphaFold model of the BUNV GP envelope is predicted, showing three hetero-hexamers fitted within both the tripod and the floor region STA. As in *Fig. 5g,h*. The wider lattice-like model of the viral envelope can be inferred from these arrangements.

Supporting Material Legend

Supplementary Material 1 BUNV Gn and Gc ectodomain AlphaFold prediction as is fitted within the BUNV tripod STA; TMDs removed as they do not comply with the STA density (represented are residues Gn 1-187, Gc 1-899).